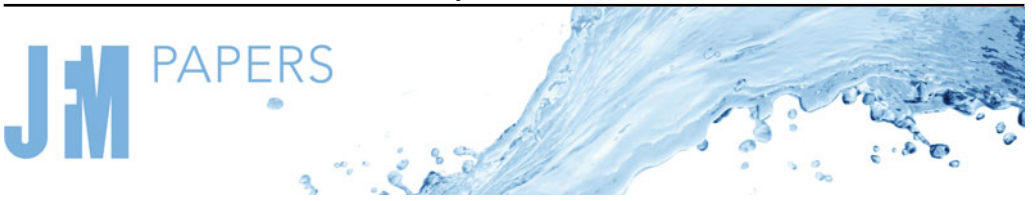
*J. Fluid Mech.* (2025), *vol.* 1024, A5, doi:10.1017/jfm.2025.10807




# Modelling external particle jet formation in explosive granular dispersal systems

**Yifeng He**[1,2], **Junsheng Zeng**[3,4], **Baolin Tian**[3,4] **and Yue Yang**[1,2]

[1]State Key Laboratory for Turbulence and Complex Systems, School of Mechanics and Engineering Science, Peking University, Beijing 100871, PR China

[2]HEDPS-CAPT, Peking University, Beijing 100871, PR China

[3]School of Aeronautic Science and Engineering, Beihang University, Beijing, PR China

[4]Shanghai Zhangjiang Institute of Mathematics, Shanghai, PR China

**Corresponding authors:** Yue Yang, yyg@pku.edu.cn; Baolin Tian, tianbaolin@buaa.edu.cn

(Received 25 March 2025; revised 28 July 2025; accepted 7 October 2025)

We investigate the evolution of an external particle jet in a dense particle bed subjected to a radially divergent air-blast. Both random and single-mode perturbations are considered. By analysing the particle dynamics, we show that the Rayleigh–Taylor instability (RTI), the Richtmyer–Meshkov instability (RMI) and large particle inertia contribute to the formation of the external jet. The external particle jet exhibits a spike-like structure at its top and a bubble-like structure near its bottom. As the expanding particle bed lowers the internal gas pressure, particles near the bubble experience strong inward coupling forces and undergo RTI with variable acceleration. Meanwhile, particles in the spike experience weak gas–particle coupling and collision forces due to large particle inertia and low particle volume fraction, respectively. Consequently, the particles in the spike retain a nearly constant velocity, in contrast to the accelerating spikes observed in cylindrical RTI. To investigate the contributions of RMI to the particle jet growth, we track the trough-near particles in the single-mode perturbation case. It is revealed that the trough-near particles accelerate under the perturbation-induced pressure gradient, overtaking the crest-near particles and inducing phase inversion, thereby resulting in an increase in jet length. We establish a linear-growth model for the jet length increment, similar to the planar Richtmyer–Meshkov impulsive model. Combined with the jet-length-increment model, we propose an external-particle-jet-length model that is consistent with both numerical and experimental results for diverse initial gas pocket central pressures and particle bed thicknesses.

**Key words:** shock waves, particle/fluid flows

https://doi.org/10.1017/jfm.2025.10807 Published online by Cambridge University Press

© The Author(s), 2025. Published by Cambridge University Press.

## 1. Introduction

High-speed multiphase flows can be found across a broad range of natural phenomena and engineering processes, such as volcanic eruptions (Lube *et al.* 2020), explosive combustion (Zhang *et al.* 2001; Balakrishnan & Menon 2010), detonations with reactive particles (Papalexandris 2004), dust dispersion (Lai, Houim & Oran 2018) and plume–surface interactions (Capecelatro 2022). Various instabilities arise in the high-speed multiphase flows, such as Kelvin–Helmholtz instability (Michael 1965), Rayleigh–Taylor instability (RTI) (Zhou 2017*a*, 2017*b*) and Richtmyer–Meshkov instability (RMI) (Zhou *et al.* 2021). In particular, the shock-driven multiphase instability (Vorobieff *et al.* 2011; McFarland *et al.* 2016; Middlebrooks *et al.* 2018), a variant of the RMI, is a typical instability for compressible flows laden with solid particles or liquid droplets (Capecelatro & Wagner 2024). It is hypothesised to be responsible for the particle jet formation in the energetic dispersal of particles when the shock is weak (Frost 2018).

The particle jet is a featured structure on the interface of a particle layer impacted by shocks. The canonical configuration for studying shock-induced interfacial instability involves a uniform shock wave impinging on a perturbed interface (Bender *et al.* 2021; Si *et al.* 2025). Recent studies have focused increasingly on the scenario where a modulated shock wave accelerates an initially unperturbed interface (Zou *et al.* 2017; He *et al.* 2023). The perturbed shock wave generates velocity perturbations near the interface (Calvo-Rivera *et al.* 2022, 2023), thereby modifying the instability growth rate (Ding *et al.* 2025).

The formation of the particle jet has been the subject of extensive experimental and numerical studies (Frost *et al.* 2012; Rodriguez *et al.* 2013, 2014; Zhang *et al.* 2015; Fernández-Godino *et al.* 2019; Hughes *et al.* 2020, 2021) because its mechanism is important in various applications, such as blast mitigation (Milne *et al.* 2014; Pontalier *et al.* 2018) and mixing of particles with air (Zhang *et al.* 2015; Posey *et al.* 2021).

The formation of distinct internal and external particle jets on the internal and external surfaces of a particle bed, respectively, was observed in experiments (Rodriguez *et al.* 2017; Xue *et al.* 2018). Following initial shock impingement on the inner interface of the particle bed, an internal particle jet develops. Later, external particle jetting forms from the outer interface of the particle bed. Xue *et al.* (2023) concluded that the morphological evolution of the dispersed particle bed is dominated by three particle-loosening events: internal particle shedding, external particle jetting and bidirectional particle fingering. Internal particle shedding originates at the internal surface, while external particle jetting initiates from the external surface. Bidirectional particle fingering occurs when finger-like jets emanate from both external and internal surfaces.

The formation of the internal particle jet has been elucidated and modelled. Xue, Sun & Bai (2016) found that the heterogeneous network of force chains plays a crucial role in the formation and evolution of the internal particle jet. Li *et al.* (2022) categorised the evolution of inward particle jetting into three distinct phases: the shock-interaction phase, the semilinear growth stage and the asymptotic growth stage. Intense interfacial transverse granular flows play an important role in the shock-interaction phase and the semilinear growth stage, while the steady diffusive pressure field dominates the asymptotic growth stage. Li *et al.* (2022) finally derived an empirical model with several fitting parameters obtained from numerical data for the internal particle jet in the planar geometry.

By contrast, the formation of the external particle jet has been described mostly qualitatively. Milne, Parrish & Worland (2010) discovered that the growth rate of the external particle jet is considerably higher than that of the classical RTI/RMI. Osnes, Vartdal & Reif (2018) demonstrated that coupling through drag is sufficient for the



https://doi.org/10.1017/jfm.2025.10807 Published online by Cambridge University Press

formation of the external particle jet. Koneru *et al.* (2020) showed that the deposition of vorticity through a gas–particle analogue of RMI plays a pivotal role in the channelling of particles into well-defined jets at the outer edge of the particle bed. Annamalai *et al.* (2016) argued that the initial perturbation in the particle volume fraction, rather than that in the detonation product, is the dominant factor in the instabilities. Xue *et al.* (2018) noted that while the external particle jet constitutes a form of RTI, the internal particle jet does not qualify as RTI due to its significantly delayed onset and slow early stage growth. Chiapolino & Saurel (2020) later found that the formation of this instability is not contingent on viscous drag effects, but rather on 'differential drag', which is modelled through non-conservative terms in the momentum and energy equations. Moreover, Chiapolino & Saurel (2020) found that the external particle jet is present in cylindrical and spherical explosions but absent in plane configurations, and therefore concluded that the radial flow divergence is important in this instability.

However, the fundamental mechanisms underlying the formation of external jets in explosive granular dispersal systems remain inadequately understood. Additionally, a comprehensive framework for modelling the evolution of these phenomena has yet to be established. In this study, we investigate the formation of an external particle jet in a two-dimensional (2-D) cylindrical particle bed subjected to air-blast loading. We quantify the length of the external particle jet and develop a generalised model to describe its evolution.

The paper is organised as follows. In § 2, we describe the numerical set-up of particle beds with initially random and single-mode perturbations. The mechanism of external particle jet formation is elucidated in § 3. Inspired by the mechanism, we develop an external-particle-jet-length model in § 4. Some conclusions are drawn in § 5.

## 2. Simulation overview

### 2.1. *Governing equations and numerical methods*

We conducted numerical simulations for explosive granular dispersal systems using the compressible multiphase particle-in-cell (CMP-PIC) method (Tian *et al.* 2020). This method integrates the Eulerian–Lagrangian approach to solve the motions of particles and gas. The two phases are fully coupled via volume fraction and momentum exchange terms, while the gas field surrounding the particle surfaces is not resolved (Capecelatro & Desjardins 2013). In the CMP-PIC method, a parcel for the particle phase consists of multiple particles with the same physical properties. The contribution of parcel $i$ to the weighted particle volume fraction is $\alpha_{p,i} = w_{i,c} V_{p,i} / V_c$, where $V_{p,i}$ denotes the volume of parcel $i$, $V_c$ the computational cell volume, and $w_{i,c}$ the distributed weight that parcel $i$ contributes to the particle volume fraction in each cell. The volume fraction of particles in a cell is $\alpha_p = \sum_i \alpha_{p,i}$, and the volume fraction of gas is $\alpha_f = 1 - \alpha_p$.

The CMP-PIC method tracks parcels in the Lagrangian framework and takes parcel–parcel interactions into account. The motion of parcels is governed by

$$\frac{\mathrm{D}\boldsymbol{x}_{p,i}}{\mathrm{D}t} = \boldsymbol{v}_{p,i} \tag{2.1}$$

and

$$\frac{\mathrm{D}\boldsymbol{v}_{p,i}}{\mathrm{D}t} = \boldsymbol{a}_{p,i} = \frac{1}{m_{p,i}} \sum_j \boldsymbol{F}_{C,ij} - \boldsymbol{S}_{p,i}. \tag{2.2}$$

Here, $\boldsymbol{a}_{p,i}$, $m_{p,i}$, $\boldsymbol{x}_{p,i}$ and $\boldsymbol{v}_{p,i}$ denote the acceleration, mass, location and velocity of parcel $i$, respectively. The collision force



https://doi.org/10.1017/jfm.2025.10807 Published online by Cambridge University Press

$$\boldsymbol{F}_{C,ij} = k_{n,p}\boldsymbol{\delta}_n + \frac{2\ln\epsilon_p}{\sqrt{\pi^2 + \ln^2\epsilon_p}}\sqrt{m_{p,i}k_{n,p}}\boldsymbol{u}_{n,ij} \tag{2.3}$$

between parcels $i$ and $j$ is calculated by a soft-sphere model (Liu, Tafti & Li 2014), where the stiffness $k_{n,p}$ and the restitution coefficient $\epsilon_p$ characterise parcel properties, and the overlap distance $\boldsymbol{\delta}_n$ with the normal velocity difference $\boldsymbol{u}_{n,ij}$ describes contact dynamics between parcels.

The source term of parcel $i$ applied by the gas phase is

$$\boldsymbol{S}_{p,i} = \frac{1}{\rho_p}\nabla p_f + D_{p,i}\left(\boldsymbol{v}_{p,i} - \boldsymbol{u}_f\right), \tag{2.4}$$

with the particle density $\rho_p$, gas pressure $p_f$ and gas velocity $\boldsymbol{u}_f$. Here, the drag force coefficient

$$D_{p,i} = C_d\frac{3\rho_f\left|\boldsymbol{v}_{p,i} - \boldsymbol{u}_f\right|}{4\rho_p d_p} \tag{2.5}$$

is calculated using the Di Felice model combined with Ergun's equation (Crowe, Sommerfield & Tsuji 1998), with the dimensionless drag coefficient

$$C_d = \frac{24}{Re_p}\begin{cases} 8.33\dfrac{\alpha_p}{\alpha_f} + 0.0972Re_p, & \alpha_f < 0.8, \\ f_{base}\alpha_f^{-\zeta}, & \alpha_f \geqslant 0.8, \end{cases} \tag{2.6}$$

standard drag factor (McGrath, Clair & Balachandar 2016)

$$f_{base} = \begin{cases} 1 + 0.167Re_p^{0.687}, & Re_p < 1000, \\ 0.0183Re_p, & Re_p \geqslant 1000, \end{cases} \tag{2.7}$$

and the exponent

$$\zeta = 3.7 - 0.65\exp\left[-\frac{1}{2}\left(1.5 - \log_{10}Re_p\right)^2\right]. \tag{2.8}$$

Here, $d_p$ is the particle diameter, $\rho_f$ the gas density, $\mu_f$ the gas viscosity, and $Re_p = \rho_f d_p\left|\boldsymbol{v}_{p,i} - \boldsymbol{u}_f\right|/\mu_f$ the particle Reynolds number. Note that specifying the valid range for the drag models is non-trivial (Osnes *et al.* 2023).

The inertial properties of particles in a fluid flow is characterised by the Stokes number

$$St = \tau_p/\tau_f, \tag{2.9}$$

where the particle response time

$$\tau_p = \frac{\rho_p d_p^2}{18\mu_f\left(1 + 0.15Re_p^{0.687}\right)} \tag{2.10}$$

is evaluated using the Schiller–Naumann correction (Berk & Coletti 2021), and the flow field characteristic time

$$\tau_f = \frac{L_\tau}{V_\tau} \tag{2.11}$$

is the ratio of the characteristic length $L_\tau$ to the characteristic velocity $V_\tau$ in the flow field.



https://doi.org/10.1017/jfm.2025.10807 Published online by Cambridge University Press

The gas phase in CMP-PIC is discretised in the Eulerian framework using four-way coupling (Wang, Liu & Yang 2020). This approach extends the two-way coupling method (Barba & Picano 2018) by additionally accounting for particle–particle collisions and the influence of particle volume fraction on the gas, while maintaining the momentum and energy transfers between gas and particles. The gas-phase governing equations (Shallcross, Fox & Capecelatro 2020)

$$\frac{\mathrm{D}\left(\alpha_f \rho_f\right)}{\mathrm{D}t} = -\alpha_f \rho_f \left(\boldsymbol{\nabla} \cdot \boldsymbol{u}_f\right), \tag{2.12}$$

$$\frac{\mathrm{D}\left(\alpha_f \rho_f \boldsymbol{u}_f\right)}{\mathrm{D}t} = -\alpha_f \rho_f \boldsymbol{u}_f \left(\boldsymbol{\nabla} \cdot \boldsymbol{u}_f\right) - \alpha_f \boldsymbol{\nabla} p_f + \sum_i \rho_{p,i} \alpha_{p,i} \boldsymbol{S}_{p,i}, \tag{2.13}$$

$$\frac{\mathrm{D}\left(\alpha_f \rho_f E_f\right)}{\mathrm{D}t} = -\alpha_f \rho_f E_f \left(\boldsymbol{\nabla} \cdot \boldsymbol{u}_f\right) - \boldsymbol{\nabla} \cdot \left(\alpha_f p_f \boldsymbol{u}_f\right) + \sum_i \rho_{p,i} \alpha_{p,i} \boldsymbol{S}_{p,i} \cdot \boldsymbol{v}_{p,i} \tag{2.14}$$

are simplified from the model of Baer & Nunziato (1986), where $\rho_{p,i}$ is the density of parcel $i$, the subscript $i$ denotes the parcel $i$ and $E_f = e + (\boldsymbol{u}_f \cdot \boldsymbol{u}_f)/2$ denotes the total energy of gas per unit volume. They are closed with the equation of state for ideal gas

$$p_f = \rho_f \frac{\mathcal{R}}{M} T = \rho_f e \left(\gamma - 1\right), \tag{2.15}$$

with the gas density $\rho_f$, ideal gas constant $\mathcal{R}$, molar mass $M$, temperature $T$, specific heat ratio $\gamma = C_p/C_v$ and internal energy $e$. Here $C_p$ and $C_v$ is the specific heat at constant pressure and constant volume respectively.

The CMP-PIC has been validated against several benchmark experiments involving shock-driven particle-laden flows (Tian *et al.* 2020), including Rogue's experiments (Rogue *et al.* 1998), the experiments conducted by Britan & Ben-Dor (2006), the cavity formation in granular media due to explosions (Zeng *et al.* 2024) and the experiments of shock-induced interfacial instability of granular media (Xue *et al.* 2018).

### 2.2. *Simulation set-up*

As sketched in figure 1(*a*), we consider a 2-D problem – a high-pressure gas pocket with radius $R_g$ expands the surrounding particle bed with initial inner radius $R_{I0}$ and outer radius $R_{O0}$. This problem is simulated in the domain $\mathcal{D} = [0, W_x] \times [0, W_y]$, with domain sizes $W_x$ and $W_y$ in the $x$- and $y$-directions. Both the gas pocket and the particle bed are set at the domain centre $(x_c, y_c) = (W_x/2, W_y/2)$. The cylindrical coordinate $(r, \theta)$ is related to the Cartesian coordinate $(x, y)$ as $r = ((x - x_c)^2 + (y - y_c)^2)^{1/2}$ and $\theta = \arctan(y - y_c, x - x_c)$. The high-pressure gas pocket is filled with still air with pressure $P_s$, density $\rho_s$ and temperature $T_s$. For the still air, we set the initial ambient pressure $P_0 = 1.013 \times 10^5$ Pa, temperature $T_0 = 299.5$ K and density $\rho_0 = P_0 M_{air}/(\mathcal{R} T_0)$ with the species molar mass $M_{air} = 29\ \mathrm{g\ mol^{-1}}$. The radius and temperature of the gas pocket are set as $R_g = 20$ mm and $T_s = 299.5$ K, respectively. Thus, the equation of state for ideal gas in (2.15) gives $\rho_s/\rho_0 = P_s/P_0$. Note that the high-pressure gas serves as the simulant agent for cylindrical bursters (Xue *et al.* 2023).

The annular particle bed with initial volume fraction $\Phi_0 = 0.6$ is filled by random distributed computational parcels (Lozano *et al.* 2016). The diameter of the parcel is set to range uniformly from 450 to 750 μm to avoid potential crystallisation during shock compaction (Xue *et al.* 2023). Note that convergence is observed as the number of particles per parcel decreases, and a single realisation is sufficient for the statistics of the particle



https://doi.org/10.1017/jfm.2025.10807 Published online by Cambridge University Press

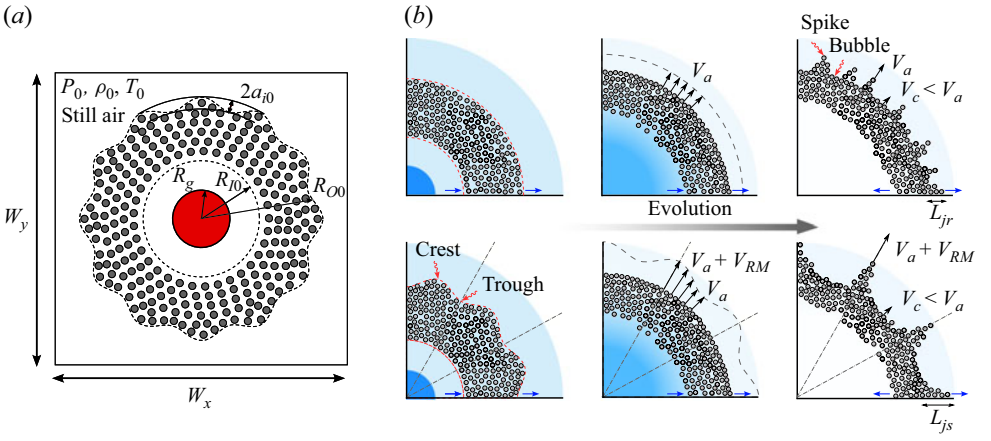



Figure 1. (*a*) Schematic of the 2-D explosive dispersal system set-up in the numerical simulation. The red circular area denotes the gas pocket with high pressure. The grey circles denote the particle bed. (*b*) Schematic for the external particle jet growth with the initial random perturbation (upper row) and the single-mode perturbation (lower row). The particle bed (grey circles) is enclosed by the red dashed line. The region is shaded based on pressure (darker areas indicate higher pressure). The blue and black arrows represent the radial flow and particle velocities, respectively.

jet length. The particle diameter $d_p = 100\,\mu\text{m}$ and gas viscosity $\mu_f = 1.92 \times 10^{-5}$ Pa s are used to calculate the particle drag force in (2.5). The restitution coefficient $\epsilon_p = 0.6$ and the normal stiffness $k_{n,p} = 5.0 \times 10^6\,\text{N m}^{-1}$ of contacts between parcels for calculating the particle collision force are set in (2.3). The restitution coefficient 0.9 and normal stiffness $O(10^6)\,\text{N m}^{-1}$ of real particles within the parcels (Renzo, Napolitano & Maio 2021) correspond to those of glass beads.

The constant initial inner radius $R_{I0} = 40\,\text{mm}$ of the particle bed is set with the thickness $h = R_{O0} - R_{I0}$. The outer interface of the particle bed is parametrised as $r = R_{O0} + a_{i0}\cos(n\theta)$, with the number $n$ of azimuthal modes and the initial amplitude $a_{i0}$ of the outer interface. The mass ratio between the surrounding particles and the gas pocket (Xue *et al.* 2023) is

$$\Gamma_M = \frac{\pi\left(R_{O0}^2 - R_{I0}^2\right)\Phi_0\rho_p}{\pi R_g^2\rho_s}. \tag{2.16}$$

The sound speed of air $c_s = \sqrt{\gamma P_0/\rho_0}$ and $h$ are used as the characteristic velocity $V_\tau$ and length $L_\tau$ of the flow field, respectively, to calculate the Stokes number. Substituting $Re_p = \rho_0 d_p c_s/\mu_f$, (2.11) and (2.10) into (2.9) yields $Re_p = 2150$ and $St = O(10)$, indicating the heavy particles here have a large inertial force compared with the drag (Li, Zeng & Xue 2023*a*). The maximum particle Mach number $Ma_p = \left|\boldsymbol{v}_{p,i} - \boldsymbol{u}_f\right|/c_s$ is approximately 1.5 in the present study. The multiphase Atwood number $A_m$ of the cases considered here is $-1$ (see (4.6)).

Two types of simulation cases, with random and single-mode perturbations, will be studied in the present study. For the random perturbation cases, we set $a_{i0} = 0\,\text{mm}$, and only vary $P_s$ and $h$. For the single-mode perturbation cases, we set $P_s = 20\,\text{bar}$ and $h = 50\,\text{mm}$, and only vary $n$ and $a_{i0}$. With grid convergence tests on the external particle jet length, the 2-D computational domain is discretised on $480 \times 480$ uniform grid points with mesh spacing $\Delta x = 1.04\,\text{mm}$. Note that due to the 2-D configuration, the volume of particle and computational cell are calculated as $\pi d_p^2/4$ and $\Delta x^2$, respectively. Each parcel



https://doi.org/10.1017/jfm.2025.10807 Published online by Cambridge University Press

corresponds to $O(100)$ particles, and over five million particles are tracked in each case. The time stepping $\Delta t$ is chosen to satisfy both the Courant–Friedrichs–Lewy condition and the time-step limit of the discrete element method (Tian *et al.* 2020). The third-order Runge–Kutta method is applied for the time integration.

The evolution of the external particle jet length is sketched in figure 1(*b*). The high-pressure gas pocket first compacts and accelerates the particle bed to a radial velocity $V_a$. The compacted particle ring inhibits atmospheric air penetration into its internal region. In the random perturbation cases (upper row), the external particle jet exhibits a spike-like structure at its top and a bubble-like structure near its bottom. As the radially expanding particle bed reduces the gas pressure inside the particle bed to below atmospheric pressure, particles near the bubble are subject to a strong radially inward gas–particle coupling force and decelerate to a radial velocity $V_c$. Meanwhile, the particles in the spike still move with $V_a$. Under this velocity difference $V_a - V_c$, the length of the external particle jet in the random perturbation cases grows to $L_{jr}$.

In the single-mode perturbation case (lower row of figure1*b*), the pressure perturbation induced by the single-mode perturbation adds a radial velocity $V_{RM}$ to the particles near the trough. Note that the trough-near particles accelerate to move faster than the crest-near particles, and then causes 'phase inversion' (Li *et al.* 2020). Then the external particle jet length in the single-mode perturbation cases grows to $L_{js} > L_{jr}$ due to the additional $V_{RM}$.

## 3. Simulation results

### 3.1. *Evolution of the external particle jet length*

The contour plot of gas pressure and position of the computational parcels are shown in figure 2. The gas pressure in the central zone decreases and the particle bed expands at $t = 2.9$ ms in both the random and single-mode perturbation cases. Similar to the classical RMI of a heavy–light interface in cylindrical geometry (Li *et al.* 2023*a*), the single-mode perturbation case finishes the phase inversion, marked by the perturbation decreasing to zero, at approximately $t = 2.9$ ms. After the gas pressure in the central zone decreases to lower than the ambient pressure, the particle jet grows at $t = 10.0$ ms in both cases. The single-mode perturbation shows a dominant-particle-jet mode protruding from the trough of the outer interface, initially near $r = R_{O0} - a_{i0}$ as in (3.9), whereas a multi-mode external particle jet grows in the random perturbation case.

To quantify the external particle jet length, we measure characteristic radii with circumferentially averaged particle volume fractions $\bar{\alpha}_p(r) = \int_0^{2\pi} \alpha_p(r, \theta)\mathrm{d}\theta/(2\pi)$. The threshold values for the inner radius $R_I$ of the particle bed, the outer radius $R_C$ of the particle bed and the outer radius of the jet zone $R_O$ are $\bar{\alpha}_p(r) = \alpha_{ps}$, $\bar{\alpha}_p(r) = \Phi_0 - \alpha_\epsilon$ and $\bar{\alpha}_p(r) = \alpha_\epsilon$, $\alpha_{ps}$ and $\alpha_\epsilon$ represent the threshold values of particle volume fraction on the inner side and outer side of the particle bed, respectively. Here, $\alpha_{ps} = 0.1$ is set for measuring the inner side of the particle bed (Rana *et al.* 2024), and $\Phi_0 = 0.6$ and $\alpha_\epsilon = 0.01$ are set in all the cases. The dashed circles in figure 2 demonstrate that the characteristic radii capture the structures of the particle bed and the external particle jet well.

Figure 3 plots the evolution of characteristic radii. When high-pressure gases are released from the gas pocket, an incident shock wave impinges on the inner surface of the particle bed, resulting in a linear growth of $R_I$, perturbed shock waves and a compaction front traversing the particle bed. The amplitude of the perturbed shock waves is comparable to the particle size. The oscillation frequency for the perturbed shock is given by $\omega_s = k_s c^+\sqrt{1 - M^{+2}}$ (Huete *et al.* 2021), where $k_s$ denotes the wavenumber, and $c^+$ and $M^+$ represent the post-shock speed of sound and Mach number, respectively. For the random perturbation case with $P_s = 20$ bar and $h = 50$ mm, the oscillation period



https://doi.org/10.1017/jfm.2025.10807 Published online by Cambridge University Press

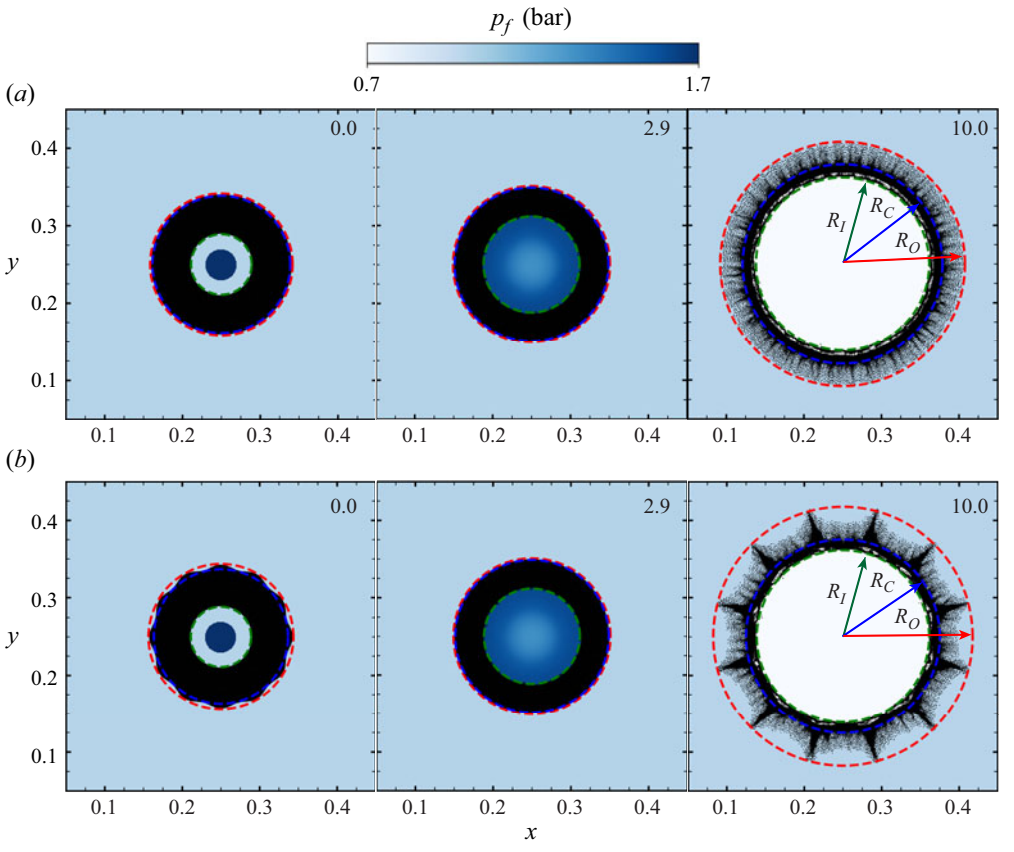



Figure 2. Evolution of the particle bed (dots) and the pressure fields (contours) in (*a*) the random perturbation case with $P_s = 20$ bar and $h = 50$ mm and (*b*) the single-mode perturbation case with $n = 12$ and $a_{i0} = 2.4$ mm. The radius of the green, blue and red circles indicate the inner radius $R_I$ of the particle bed, the outer radius $R_C$ of the particle bed and the outer radius $R_O$ of the jet zone, respectively. The numbers in the upper right corner denote the time in ms. The unit of the axes is m.

$T_s = 2\pi/\omega_s$ for the perturbed shock is approximately 0.2 µs by adopting $k_s = 2\pi/d_p$, $c^+ = 500\ \mathrm{m\ s^{-1}}$ and $M^+ = 0.1$. The time interval for the shock passing through the particle bed is approximately 100 µs, exceeding the oscillation period by two orders of magnitude. Consequently, the perturbed amplitude of the incident shock introduced by randomly distributed particles rapidly diminishes. After the compaction front reaches the outer surface of the particle bed at approximately $t = 2$ ms, $R_O$ and $R_C$ start to grow. In both the random and single-mode perturbation cases, $R_C$ experiences a short period of linear growth and the growth is mitigated at approximately $t = 3$ ms due to strong inward gas–particle coupling forces. Moreover, the evolutionary trends of $R_I$, $R_O$ and $R_C$ are very similar in both cases.

The external particle jet length

$$L_{j\Psi} = R_O - R_C, \quad \Psi = r, s \tag{3.1}$$

is defined as the outer radius difference between the particle bed and the top of the jet, where subscripts $r$ and $s$ denote the random and single-mode perturbation cases, respectively. The evolution of $L_{jr}$ and $L_{js}$ is plotted in figure 4. All the random and single-mode perturbation cases undergo a compression stage until the critical time $t = t_c$,



https://doi.org/10.1017/jfm.2025.10807 Published online by Cambridge University Press

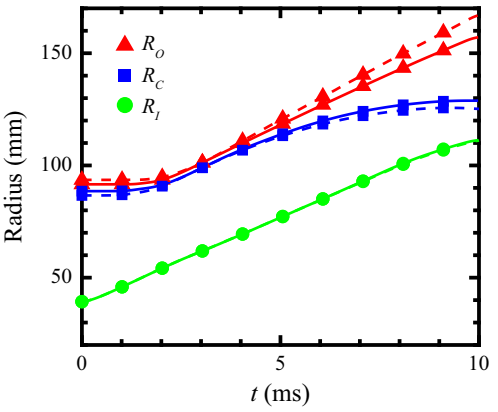



Figure 3. Evolution of characteristic radii in the random perturbation case with $P_s = 20$ bar and $h = 50$ mm (solid lines) and the single-mode perturbation case with $n = 12$ and $a_{i0} = 2.4$ mm (dashed lines).

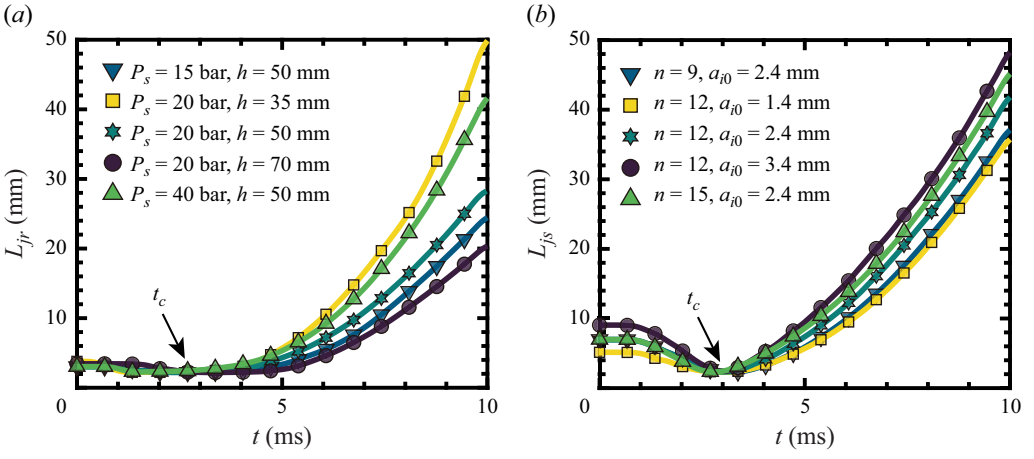



Figure 4. Evolution of the particle jet length in (*a*) the random perturbation cases and (*b*) the single-mode perturbation cases with various parameters.

when the jet length reaches its minimum value. They then enter a nonlinear growth stage. In the random perturbation cases, $L_{jr}$ grows faster with larger $P_s$ and smaller $h$. This is because the particle bed expands more rapidly under these conditions, accelerating $R_O$ and causing a quicker decline in $p_f$ in the central zone, which in turn strongly decelerates the growth of $R_C$. In the single-mode perturbation cases, $L_{js}$ grows faster with larger $n$ and $a_{i0}$ because faster growth of $R_O$ results from stronger pressure perturbations induced by the larger $n$ and $a_{i0}$. The effects of parameters on $L_{jr}$ and $L_{js}$ will be discussed further in § 4.

To investigate the single-mode perturbation's effects on the growth of the particle jet length, we introduce the jet length increment $\Delta L_j = L_{js} - L^*_{jr}$, where $L^*_{jr}$ and $L_{js}$ denote the particle jet length of the random perturbation case with $P_s = 20$ bar and $h = 50$ mm and the single-mode perturbation cases with the same $P_s$ and $h$, respectively. In figure 5, $\Delta L_j$ firstly experiences the compression stage because the particles initially near the trough accelerate to move faster than those initially near the crests. After the phase inversion at $t = t_m$ (listed in table 1), $\Delta L_j$ experiences a linear growth, which is similar to that observed in the linear stage of planar RMI (Richtmyer 1960; Meshkov 1969) and



https://doi.org/10.1017/jfm.2025.10807 Published online by Cambridge University Press

| Case | $\Gamma_M$ | $P_s$ (bar) | $h$ (mm) | $L_{jr}(t_c)$ (mm) | $k$ (mm$^{-1}$) | $a_{i0}$ (mm) | $t_m$ (ms) |
|---|---|---|---|---|---|---|---|
| $P_s = 15$ bar and $h = 50$ mm | 1354 | 15 | 50 | 2.4 | – | 0 | – |
| $P_s = 20$ bar and $h = 35$ mm | 629 | 20 | 35 | 2.3 | – | 0 | – |
| $P_s = 20$ bar and $h = 50$ mm | 1016 | 20 | 50 | 2.4 | – | 0 | – |
| $P_s = 20$ bar and $h = 70$ mm | 1641 | 20 | 70 | 2.7 | – | 0 | – |
| $P_s = 40$ bar and $h = 50$ mm | 508 | 40 | 50 | 2.7 | – | 0 | – |
| $n = 9$ and $a_{i0} = 2.4$ mm | 1016 | 20 | 50 | 2.4 | 0.100 | 2.4 | 3.3 |
| $n = 12$ and $a_{i0} = 1.4$ mm | 1016 | 20 | 50 | 2.4 | 0.133 | 1.4 | 3.0 |
| $n = 12$ and $a_{i0} = 2.4$ mm | 1016 | 20 | 50 | 2.4 | 0.133 | 2.4 | 3.0 |
| $n = 12$ and $a_{i0} = 3.4$ mm | 1016 | 20 | 50 | 2.4 | 0.133 | 3.4 | 3.0 |
| $n = 15$ and $a_{i0} = 2.4$ mm | 1016 | 20 | 50 | 2.4 | 0.167 | 2.4 | 2.8 |

Table 1. Summary of parameters in random and single-mode perturbation cases. Additionally, $R_{I0} = 40$ mm, $R_{g0} = 20$ mm and $\Phi_0 = 0.6$ are set in all cases. The wave number is $k = n/R_{O0}$.

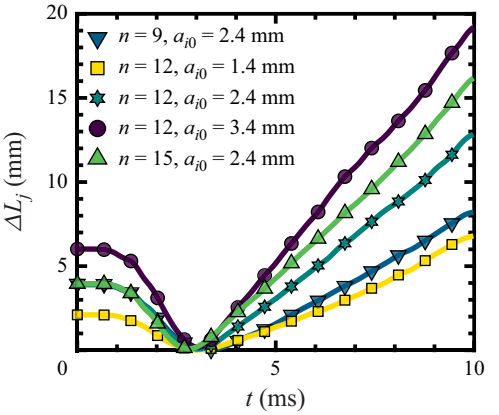



Figure 5. Evolution of the particle jet length increment in the single-mode perturbation cases with various parameters.

is distinct from the nonlinear growth of the cylindrical RMI (Bell 1951; Mikaelian 2005; Ding *et al.* 2017).

### 3.2. *Formation of the external particle jet*

As sketched in figure 6(*a*), we measure the averaged particles' quantities at the compaction ($C$) zone within $R_C - 0.1h < r < R_C$ and near the outer ($O$) zone within $|r_0 - R_{O0}| < \Delta x$ to characterise the external particle jet growth, where $r_0$ denotes the radial coordinate $r$ at the initial time $t = 0$. The random perturbation case with $P_s = 20$ bar and $h = 50$ mm is studied here. We calculate the mass-weighted averaged radial components of coordinate, velocity and acceleration

$$\bar{f}_{pr,\Omega} = \frac{\sum_{i\in\Omega} \rho_p \alpha_{p,i} f_{pr,i}}{\sum_{i\in\Omega} \rho_p \alpha_{p,i}}, \quad f = r,\, v,\, a \text{ and } \Omega = C,\, O \tag{3.2}$$

of particles at the compaction and outer zones, where $\rho_p$ and $\alpha_{p,i}$ are the particle density and particle volume fraction, respectively.

Figure 6(*b*) shows that the radii

$$\hat{R}_{pr,\Omega}(t) = \bar{r}_{pr,\Omega}(t = 0) + \int_0^t \bar{v}_{pr,\Omega}(\tau)\mathrm{d}\tau, \quad \Omega = C,\, O \tag{3.3}$$



https://doi.org/10.1017/jfm.2025.10807 Published online by Cambridge University Press

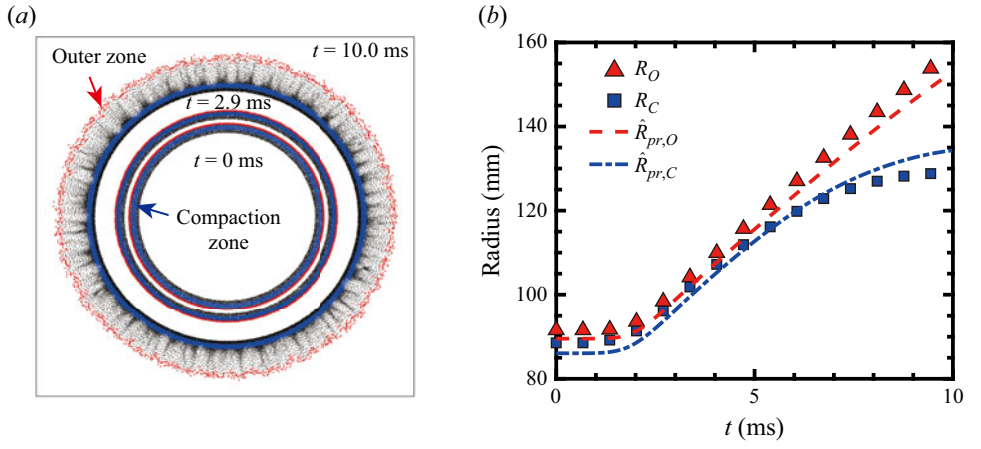



Figure 6. (*a*) Evolution of particles in the random perturbation case with $P_s = 20$ bar and $h = 50$ mm. The red and blue dots represent particles in the outer and compaction zones, respectively. (*b*) Evolution of the characteristic radii (symbols) and the radii integrated from the averaged velocity of the outer and compaction zones (lines).

integrated from the average velocity of the compaction and outer zones are close to the characteristic radii, i.e. $\hat{R}_{pr,\Omega} \approx R_\Omega$. Thus, the growth rate

$$\frac{\mathrm{d}L_{jr}}{\mathrm{d}t} = \frac{d\,(R_O - R_C)}{\mathrm{d}t} \approx \frac{d\big(\hat{R}_{pr,O} - \hat{R}_{pr,C}\big)}{\mathrm{d}t} = \bar{v}_{pr,O} - \bar{v}_{pr,C} \tag{3.4}$$

of the external particle jet length can be approximated as the difference between average radial velocities of particles in compaction and outer zones.

According to (3.4), we further study the evolution of $\bar{v}_{pr,O}$ and $\bar{v}_{pr,C}$. Figure 7(*a*) shows that the velocities

$$\hat{v}_{pr,\Omega}(t) = \bar{v}_{pr,\Omega}(t=0) + \int_0^t \bar{a}_{pr,\Omega}(\tau)\mathrm{d}\tau, \quad \Omega = C,\, O \tag{3.5}$$

integrated from the averaged accelerations agree well with the averaged velocities $\bar{v}_{pr,O}$ and $\bar{v}_{pr,C}$. From (2.2), the $r$-acceleration of parcel $i$ is contributed from the drag, pressure and collision as

$$a_{pr,i} = \underbrace{D_{p,i}\left(\boldsymbol{v}_{pr,i} - \boldsymbol{u}_{fr}\right)}_{Drag,\, a_{idr}} \underbrace{- \frac{1}{\rho_p}\partial_r p_f}_{Pressure,\, a_{ipr}} + \underbrace{\frac{1}{m_{p,i}}\sum_j F_{Cr,ij}}_{Collision,\, a_{icr}}. \tag{3.6}$$

Thus, the mass-weighted averaged acceleration of particles in the outer and compaction zones can be rewritten as

$$\bar{a}_{pr,\Omega}(t) = \bar{a}_{idr,\Omega} + \bar{a}_{ipr,\Omega} + \bar{a}_{icr,\Omega}, \quad \Omega = C,\, O, \tag{3.7}$$

then the integrating velocity $\hat{v}_{pr}$ in (3.5) can be decomposed as

$$\hat{v}_{pr,\Omega}(t) = \underbrace{\int_0^t \bar{a}_{idr,\Omega}\,\mathrm{d}t}_{drag,\, \hat{v}_{idr}} + \underbrace{\int_0^t \bar{a}_{ipr,\Omega}\,\mathrm{d}t}_{pressure,\, \hat{v}_{ipr}} + \underbrace{\int_0^t \bar{a}_{icr,\Omega}\,\mathrm{d}t}_{collision,\, \hat{v}_{icr}}, \quad \Omega = C,\, O, \tag{3.8}$$

with $\bar{v}_{pr,\Omega}(t=0) = 0$.



https://doi.org/10.1017/jfm.2025.10807 Published online by Cambridge University Press

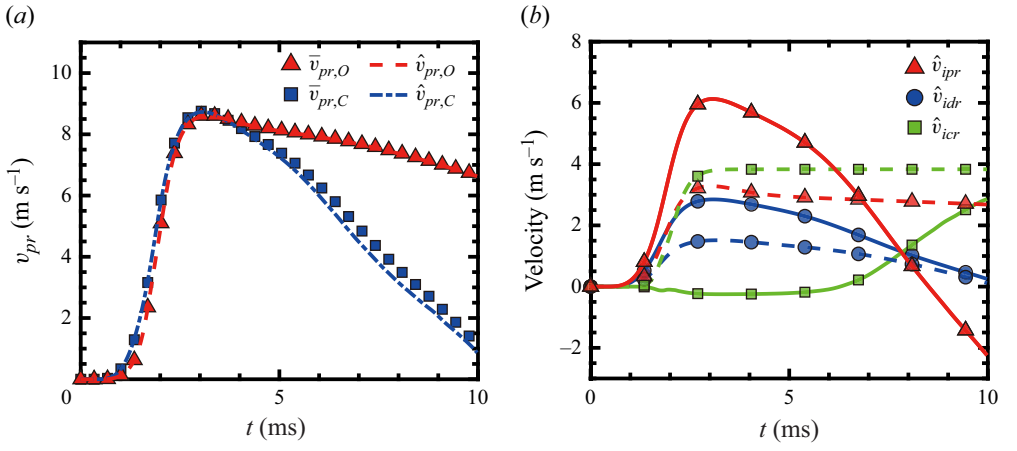



Figure 7. (*a*) Comparisons of the averaged velocity $\bar{v}_{pr}$ in (3.2) and integrating velocity $\hat{v}_{pr}$ in (3.5) in the random perturbation case with $P_s = 20$ bar and $h = 50$ mm. (*b*) Evolution of budgets of $\hat{v}_{pr}$ in the outer zone (dashed lines) and compaction zone (solid lines).

Figure 7(*b*) plots the evolution of budgets of $\hat{v}_{pr}$. In the compaction zone, the pressure and drag terms first increase $\hat{v}_{pr,C}$ before $t = 2.9$ ms, and then decrease $\hat{v}_{pr,C}$ dramatically. Thus, particles in the compaction zone experience strong inward gas–particle coupling forces and undergo RTI with variable acceleration. In addition, the collision term has negligible effects on the variation of $\hat{v}_{pr,C}$ before $t = 2.9$ ms, and then increases $\hat{v}_{pr,C}$.

In the outer zone, the pressure and collision terms first increase $\hat{v}_{pr,O}$ before $t = 2.9$ ms, and then they have negligible effects on the variation of $\hat{v}_{pr,O}$, due to the large particle inertia and small particle volume fraction, respectively. In addition, the drag term increases $\hat{v}_{pr,O}$ before $t = 2.9$ ms, and then slightly decreases $\hat{v}_{pr,O}$. Thus, RTI controls radial deceleration in the compaction zone, while large particle inertia keeps near-constant radial velocity in the outer zone, enabling faster movement of outer particles and promoting external jet growth.

### 3.3. *Effects of RMI on the jet length increment*

Since the growth of jet length increment is analogous to that of planar RMI (Peng, Yang & Xiao 2021*a*, 2021*b*), we examine the effects of RMI on the jet length increment. To investigate the contributions of RMI on the particle jet growth, we track the motion of particles, which are initially near the trough ($T$) and waist ($W$) points. The trough, waist and crest points (see figure 1) are at the radial coordinates

$$r_T = R_{O0} - a_{i0}, \quad \theta_T = \frac{(2i+1)\,\pi}{n}, \quad i = 0, \ldots, n-1, \tag{3.9}$$

$$r_W = R_{O0}, \quad \theta_W = \frac{(4i \pm 1)\,\pi}{2n}, \quad i = 0, \ldots, n-1 \tag{3.10}$$

and

$$r_{crest} = R_{O0} + a_{i0}, \quad \theta_{crest} = \frac{2i\pi}{n}, \quad i = 0, \ldots, n-1, \tag{3.11}$$

respectively. The waist-near particles satisfy $|r_0 - r_W| < \Delta x$ and $|\theta_0 - \theta_W| < 0.01\pi$. The trough-near particles are initially in the disk region of radius $R_{TN} = \Delta x$ centring at



https://doi.org/10.1017/jfm.2025.10807 Published online by Cambridge University Press

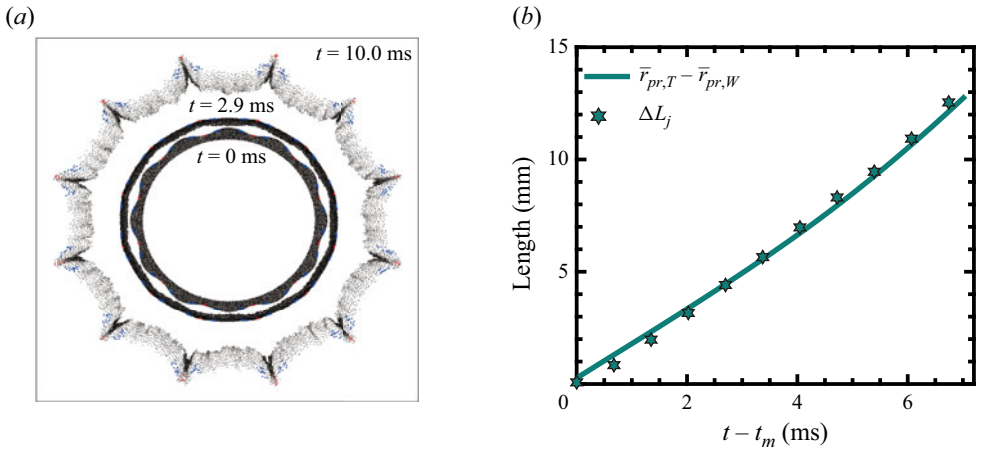



Figure 8. (*a*) Evolution of particles in the single-mode perturbation case with $n = 12$ and $a_{i0} = 2.4$ mm. The initially trough-near (red dots) and waist-near (blue dots) particles are tracked in a Lagrangian framework. (*b*) Evolution of the jet length increment $\Delta L_j$ (symbols) and $\bar{r}_{pr,T} - \bar{r}_{pr,W}$ (lines).

the trough point. The single-mode perturbation case with $n = 12$ and $a_{i0} = 2.4$ mm is studied here. The mass-weighted averaged radial components of coordinate, velocity and acceleration

$$\bar{f}_{pr,\Omega} = \frac{\sum_{i\in\Omega} \rho_p \alpha_{p,i} f_{pr,i}}{\sum_{i\in\Omega} \rho_p \alpha_{p,i}}, \quad f = r,\, v,\, a \text{ and } \Omega = T,\, W, \tag{3.12}$$

of the trough-near ($T$) and waist-near ($W$) particles are calculated.

The jet length can be represented by $\bar{r}_{pr,T}$ and $\bar{r}_{pr,W}$. Figure 8(*a*) shows that the trough-near particles (red dots) are at the outermost part of the particle ring during $t > 2.9$ ms, i.e. $R_O \approx \bar{r}_{pr,T}$ during the growth stage. Thus, combining with (3.1), the jet length in the single-mode perturbation case with $n = 12$ and $a_{i0} = 2.4$ mm can be rewritten as

$$L_{js} \approx \bar{r}_{pr,T} - R_C = \left(\bar{r}_{pr,T} - \bar{r}_{pr,W}\right) + \left(\bar{r}_{pr,W} - R_C\right). \tag{3.13}$$

Meanwhile, the definition of $\Delta L_j$ suggests

$$L_{js} = \Delta L_j + L^*_{jr} \tag{3.14}$$

in the random perturbed case with $P_s = 20$ bar and $h = 50$ mm. Figure 8(*b*) shows that $\bar{r}_{pr,T} - \bar{r}_{pr,W} \approx \Delta L_j$, hence the radial velocity difference between the trough-near and waist-near particles induced by the single-mode perturbation increases $\Delta L_j$. Besides, the variation rate of $\Delta L_j$ is approximated by

$$\Delta \dot{L}_j = \mathrm{d}\Delta L_j/\mathrm{d}t \approx \dot{\bar{r}}_{pr,T} - \dot{\bar{r}}_{pr,W} = \bar{v}_{pr,T} - \bar{v}_{pr,W}. \tag{3.15}$$

Thus, we need to further study the evolution of $\bar{v}_{pr,T}$ and $\bar{v}_{pr,W}$.

Figure 9(*a*) shows that both $\bar{v}_{pr,T}$ and $\bar{v}_{pr,W}$ accelerate before $t = 2.9$ ms, then decelerate slightly due to the large particle inertia. During the acceleration stage, the trough-near particles accelerates to move faster than the waist-near and crest-near particles, and then cause phase inversion.

The mass-weighted averaged velocity of the trough-near and waist-near particles can be rewritten as (He *et al.* 2024)

$$\bar{v}_{pr,\Omega}(t) = \bar{v}_{idr,\Omega} + \bar{v}_{ipr,\Omega} + \bar{v}_{icr,\Omega}, \quad \Omega = T,\, W, \tag{3.16}$$



https://doi.org/10.1017/jfm.2025.10807 Published online by Cambridge University Press

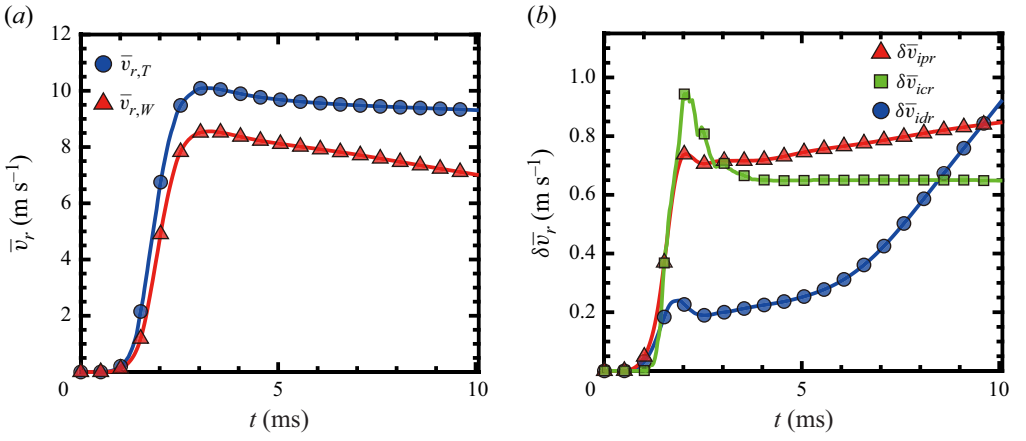



Figure 9. Evolution of (*a*) the averaged velocity $\bar{v}_r$ of trough-near and waist-near particles and (*b*) budgets of $\delta\hat{v}_r$ in the single-mode perturbation case with $n = 12$ and $a_{i0} = 2.4$ mm.

where $\bar{v}_{idr,\Omega}$, $\bar{v}_{ipr,\Omega}$ and $\bar{v}_{icr,\Omega}$ denote the drag, pressure and collision terms, respectively, and $\bar{v}_{pr,\Omega} = 0$ at $t = 0$.

Combining (3.15) and (3.16) yields the decomposition

$$\Delta\dot{L}_j = \delta\bar{v}_r = \underbrace{\left(\bar{v}_{idr,T} - \bar{v}_{idr,W}\right)}_{Drag,\ \delta\bar{v}_{idr}} - \underbrace{\left(\bar{v}_{ipr,T} - \bar{v}_{ipr,W}\right)}_{Pressure,\ \delta\bar{v}_{ipr}} + \underbrace{\left(\bar{v}_{icr,T} - \bar{v}_{icr,W}\right)}_{Collision,\ \delta\bar{v}_{icr}}, \tag{3.17}$$

where $\delta$ denotes the velocity difference at the trough and waist. Figure 9(*b*) plots the evolution of budgets of $\delta\bar{v}_r$. During the acceleration stage before $t = 2.9$ ms, the velocity difference $\delta\bar{v}_r$ is mainly contributed from collision and pressure terms. At the late stage, the drag term slightly increases $\delta\bar{v}_r$ due to large particle inertia. Due to the small particle volume fraction near the spike, the effects of the collision and pressure on $\delta\bar{v}_r$ is minor at the late stage. Therefore, the jet length increment (shown in figure 5) grows nearly linearly primarily because of the large particle inertia and small particle volume fraction.

Since the collision and pressure terms dominate the generation of $\delta\bar{v}_r$, the gas–particle mixture can be viewed as a continuum during the acceleration stage. Thus, the single-mode perturbation triggers RMI, generating $\delta\bar{v}_r$ and $\Delta L_j$. Note that the RMI in the random perturbation cases is negligible due to the small initial interfacial amplitude. The mode coupling effects on jet formation are discussed in Appendix A.

## 4. Modelling of the external particle jet

### 4.1. *Jet-length-increment model*

Inspired by the mechanism of the interfacial instability, we model the linear growth rate of the jet length increment. Richtmyer (1960) developed a

$$\dot{a}_i = k a_{i0}^{+} A^{+} \Delta U \tag{4.1}$$

for a gas interface with perturbation amplitude $a_i$ subjected to a shock, where $a_{i0}^{+}$, $A^{+}$ and $\Delta U$ are the post-shock perturbed amplitudes of the interface, Atwood number and average velocity difference of the gas around the interface, respectively. Ukai, Balakrishnan & Menon (2010) developed a linear-growth model

$$\dot{a}_i = k a_{i0} A_m \Delta U \tag{4.2}$$



https://doi.org/10.1017/jfm.2025.10807 Published online by Cambridge University Press

for the gas-phase interface surrounded by particles subjected to a shock, with introducing the multiphase Atwood number $A_m$. Throughout the growth of external particle jets, the particle Mach number $Ma_p$ maintains values below 0.4, demonstrating negligible compressibility effects during this stage (Loth 2008). Here we treat the gas–particle mixture as a continuum, and then propose a linear-growth model (detailed derivations are provided in Appendix B)

$$\Delta \dot{L}_j = \dot{a}_i = k a_{i0} \left| A_m \right| \Delta U_m \tag{4.3}$$

for the jet length increment by adopting the multiphase Atwood number (Ukai *et al.* 2010)

$$A_m = \frac{\left(\rho_{f2}\alpha_{f2} + \rho_{p2}\alpha_{p2}\right) - \left(\rho_{f1}\alpha_{f1} + \rho_{p1}\alpha_{p1}\right)}{\left(\rho_{f2}\alpha_{f2} + \rho_{p2}\alpha_{p2}\right) + \left(\rho_{f1}\alpha_{f1} + \rho_{p1}\alpha_{p1}\right)}. \tag{4.4}$$

Since the driving blast is extremely complex, modelling the post-shock averaged velocity difference $\Delta U_m$ is difficult. Thus, we assume that $\Delta U_m$ is a constant during the acceleration stage. Integrating (4.3) from $t = t_m$ when the phase inversion completes to a given time $t$ yields

$$\Delta L_j = k a_{i0} \left| A_m \right| \Delta U_m \left(t - t_m\right), \tag{4.5}$$

with the wavenumber $k = n/R_{O0}$. In (4.5), $t_m$ is extracted from numerical data in the present study, and can be also approximated by $t_m = 2a_{i0}/\dot{a}_i$ (see (4.3)) in practice. The parameters used in the comparison between the model and simulation results are listed in table 1.

Given $\rho_{f1} = \rho_{f2} = \rho_0$, $\rho_{p1} = \rho_{p2} = \rho_p$, $\alpha_{f1} = (1 - \Phi_0)$, $\alpha_{f2} = 1$, $\alpha_{p1} = \Phi_0$, $\alpha_{p2} = 0$, $\Phi_0 = 0.6$ and $\rho_p/\rho_0 = O(10^3)$ in the present parameters, (4.4) becomes

$$A_m = \frac{\rho_0 - \rho_p\Phi_0 - \rho_0(1 - \Phi_0)}{\rho_0 + \rho_p\Phi_0 + \rho_0(1 - \Phi_0)} \approx -1. \tag{4.6}$$

Additionally, $\Delta U_m = 5.6\,\mathrm{m\,s^{-1}}$ is fitted from the single-mode perturbation case with $n = 15$ and $a_{i0} = 2.4\,\mathrm{mm}$. Note that a detailed modelling of $\Delta U_m$ should be considered in the future.

Figure 10 demonstrates that the model in (4.5) well captures the linear growth of $\Delta L_j$ in the single-mode perturbation cases at various $n$ and $a_{i0}$, where the model estimation generally agrees with the simulation result. With larger $n$ and $a_{i0}$, $\Delta L_j$ grows faster due to a larger pressure perturbation in the RMI. Note that the model does not incorporate drag effects, because the drag term has minor effects at the early stage (see figure 9*b*).

### 4.2. *External-particle-jet-length model*

Now we model the external particle jet length $L_{jr}$ in the random perturbed cases. As sketched in figure 11, three characteristic radii, $R_I$, $R_C$ and $R_O$, separate four zones: the central zone, the particle bed, the external particle jet and the outer zone. First, the high-pressure gas in the central zone accelerates the particle bed radially outward. Subsequently, the pressure in the central zone decreases to below ambient pressure, and the external particle jet grows.

The external particle jet starts to grow at the initial time when $a_c$ is the deceleration of particles near $r = R_C$ begin to shed from the outer surface of the particle bed. The initial time of the external-particle-jet-length model is approximated by the critical time

$$t_c \approx \frac{h}{V_{CF}}, \tag{4.7}$$



https://doi.org/10.1017/jfm.2025.10807 Published online by Cambridge University Press

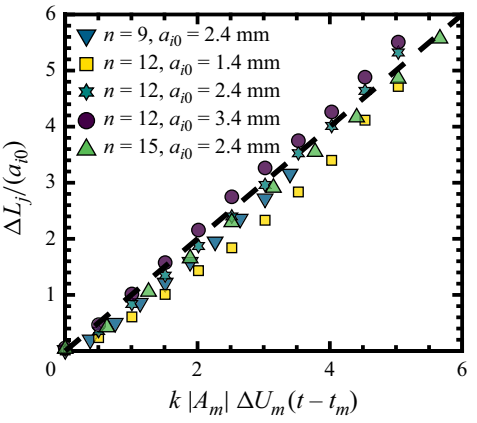



Figure 10. Evolution of the jet length increment in the single-mode perturbation case from numerical simulation (symbols) and modelling (dashed line) results at various $n$ and $a_{i0}$.

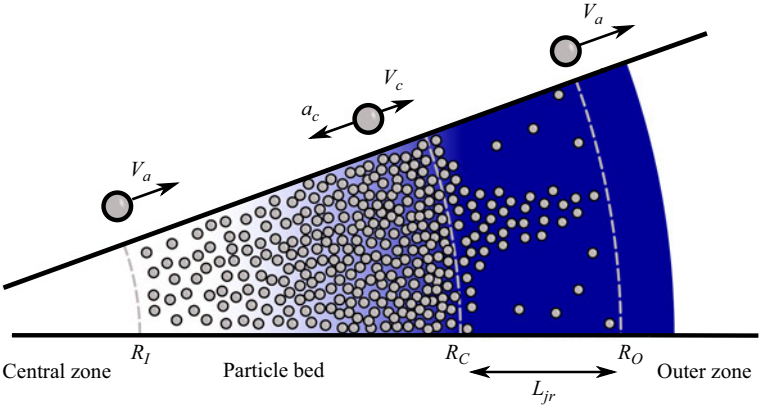



Figure 11. Schematic for the external particle jet growth in the random perturbation case. The gas pressure in the central zone is lower than the ambient pressure in the jet zone and the outer zone.

when the jet length reaches minimum and the compaction front reaches the outer surface of the particle bed.

In (4.7), the propagation velocity

$$V_{CF} = \sqrt{\frac{P_r - P_0}{\rho_p} \frac{\Phi_{comp}}{\left(\Phi_{comp} - \Phi_0\right)\Phi_0}} \tag{4.8}$$

of the compaction front is evaluated by the model proposed by Xue *et al.* (2023), where the volume fraction of the 2-D compacted particle bed is set to be $\Phi_{comp} = 0.8$, and the pressure exerting on the inner surfaces of the particle bed is estimated by $P_r = P_s R_g^2 / R_{I0}^2$. Note that $\Phi_{comp}$ is influenced by both $\Phi_0$ and the strength of the blast wave (Li *et al.* 2023*b*).



https://doi.org/10.1017/jfm.2025.10807 Published online by Cambridge University Press

At $t = t_c$, the radial velocity

$$V_a = F\left(\Phi_0, \Gamma_M\right)\sqrt{\frac{2e_{gas}}{\frac{\Gamma_M}{0.2\rho_p^{0.18}} + 0.5}} \tag{4.9}$$

of the particle bed is estimated by a modified Gurney equation (Milne 2016), with the correction function

$$F\left(\Phi_0, \Gamma_M\right) = 1 + \left[0.162\exp\left(1.127\Phi_0\right) - 0.5\right]\log_{10}(\Gamma_M) \tag{4.10}$$

and the energy per unit mass

$$e_{gas} = \frac{\left(P_s - P_0\right)}{\left(\gamma - 1\right)\rho_0} \tag{4.11}$$

of the gas pocket (Crowl 2003).

At the intersection between the central zone and the particle bed with $r = R_I$, the particles are subject to drag, pressure gradient and collision forces, which are weak due to the large particle inertia and small particle volume fraction. Therefore, we assume that the particles in the vicinity of $r = R_I$ move with a time-invariant radial velocity $V_a$. Namely,

$$R_I(t) = R_{I0} + \int_0^t V_a \mathrm{d}\tau \tag{4.12}$$

experiences approximately linear growth (see figure 3).

The exterior of the particle bed is characterised by the compaction of particles and a relatively low radial velocity of the gas. Consequently, we assume that mass transfer between the central and outer zones is insignificant. The average gas pressure $\bar{P}_C$ in the central zone decreases mainly due to the expansion of the particle bed. Neglecting the gas leakage and assuming that the gas in the central zone undergoes isothermal expansion, we obtain

$$\bar{P}_C(t) \approx \frac{\bar{P}_C(t_c)R_I^2(t_c)}{R_I^2(t)}. \tag{4.13}$$

The particles in the particle bed decelerate due to the radial inward pressure gradient. Thus, at $t = t_c$, we assume that the average pressure $\bar{P}_c$ in the central zone in (4.13) is equal to the ambient pressure $P_0$. The outer zone constitutes air with an approximate ambient pressure of $P_0$. The gas pressure in the jetting zone is also approximately equal to $P_0$ due to the low particle volume fraction.

Due to the large particle inertia and small particle volume fraction (see figure 7), it can thus be assumed that the particles in the vicinity of $r = R_O$ move with a time-invariant radial velocity $V_a$, which is approximated as

$$R_O(t) = R_O(t_c) + \int_{t_c}^t V_a \mathrm{d}\tau, \tag{4.14}$$

i.e. $R_O$ also experiences approximately linear growth (see figure 3).

The particles situated in close proximity to the junction $r = R_C$ of the particle bed and the jetting zone move with a radial velocity $V_c$, which is described by

$$R_C(t) = R_C(t_c) + \int_{t_c}^t V_c(\tau)\mathrm{d}\tau. \tag{4.15}$$



https://doi.org/10.1017/jfm.2025.10807 Published online by Cambridge University Press

Particles in this region exhibit a compacted state (see figure 6), accompanied by a notable gas-pressure gradient and deceleration

$$a_c(t) = \beta \frac{P_0 - \bar{P}_C(t)}{h_c \rho_p}, \tag{4.16}$$

where $\beta$ is the fitting parameter related to the property of blast, and $\bar{P}_c(t)$ is calculated by (4.13). Thus, $V_c$ in (4.15) evolves as

$$V_c(t) = V_a - \int_{t_c}^{t} a_c(\tau) \mathrm{d}\tau. \tag{4.17}$$

The thickness $h_c$ of the compacted particle bed in (4.16) is obtained by the particle volume conservation:

$$\Phi_{comp}\left[(h_c + R_I(t_c))^2 - R_I^2(t_c)\right] = \Phi_0\left[(h + R_{I0})^2 - R_{I0}^2\right], \tag{4.18}$$

where $R_I(t_c) = R_{I0} + V_a t_c$ is obtained by substituting $t = t_c$ into (4.12).

Substituting (4.12)–(4.18) into (3.1) yields the growth of external particle jet length for the random perturbation cases:

$$L_{jr}(t) - L_{jr}(t_c) = \int_{t_c}^{t} \int_{t_c}^{\tau} a_c\,(\xi)\,\mathrm{d}\xi \mathrm{d}\tau = \frac{\beta P_0}{h_c \rho_p} \int_{t_c}^{t} \int_{t_c}^{\tau} \left(1 - \frac{R_I^2(t_c)}{(R_I(t_c) + V_a \xi)^2}\right) \mathrm{d}\xi \mathrm{d}\tau, \tag{4.19}$$

where $\xi$ is a dummy variable sharing the same dimension as time $t$, and then

$$\begin{aligned} L_{jr}(t) =& L_{jr}(t_c) + \beta \frac{P_0}{h_c \rho_p} \left[ \frac{(t - t_c)^2}{2} + \left(\frac{R_{I0} + V_a t_c}{V_a}\right)^2 \ln\left(\frac{R_{I0} + V_a\,(t + t_c)}{R_{I0} + 2V_a t_c}\right) \right. \\ & \left. - \frac{(R_{I0} + V_a t_c)^2}{V_a} \frac{(t - t_c)}{R_{I0} + 2V_a t_c} \right], \end{aligned} \tag{4.20}$$

where $t_c$, $V_a$ and $h_c$ are calculated by (4.7), (4.9) and (4.18), respectively. Similarly, substituting (4.5) and (4.20) into (3.14) yields the growth model of the external particle jet length for the single-mode perturbation cases:

$$\begin{aligned} L_{js}(t) =& L_{jr}(t_c) + \beta \frac{P_0}{h_c \rho_p} \left[ \frac{(t - t_c)^2}{2} + \left(\frac{R_{I0} + V_a t_c}{V_a}\right)^2 \ln\left(\frac{R_{I0} + V_a\,(t + t_c)}{R_{I0} + 2V_a t_c}\right) \right. \\ & \left. - \frac{(R_{I0} + V_a t_c)^2}{V_a} \frac{(t - t_c)}{R_{I0} + 2V_a t_c} \right] + k a_{i0}\,|A_m|\,\Delta U_m\,(t - t_m)\,. \end{aligned} \tag{4.21}$$

Figure 12 shows that the model results in (4.20) and (4.21) generally agree with the simulation results. Note that the fitting parameter $\beta = 1.0$ is set, and parameters used in the comparison are listed in table 1. Figure 12(*a*) demonstrates that the model in (4.20) well captures the growth of $L_{jr}$ in the random perturbation cases at moderate $P_s$ and $h$. Compared with a thicker particle bed with the same $P_s$, the particle bed with smaller $h$ moves with larger radial velocity $V_a$ due to lower mass ratio $\Gamma_M$, and then the gas pressure $\bar{P}_C$ in the central zone decreases faster. Due to the faster decreasing $\bar{P}_C$, the particle bed with smaller $h$ is subjected to larger $a_c$, and then $L_{jr}$ grows faster. Compared with the cases with the same $h$, the cases with larger $P_s$ also generate larger radial velocity $V_a$ due to lower mass ratio $\Gamma_M$, and also induce faster growth of $L_{jr}$. The model underestimates



https://doi.org/10.1017/jfm.2025.10807 Published online by Cambridge University Press

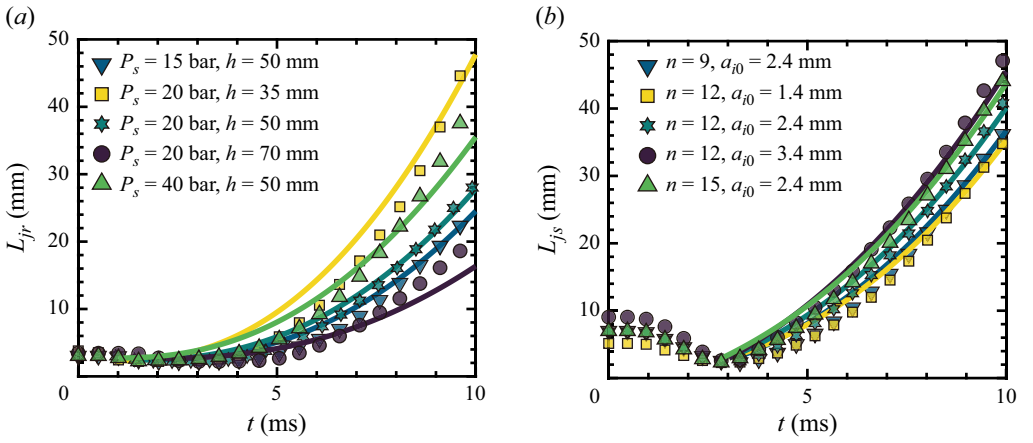



Figure 12. Evolution of the particle jet length in (*a*) random perturbation cases and (*b*) single-mode perturbation cases from numerical simulation (symbols) and modelling (lines) results.

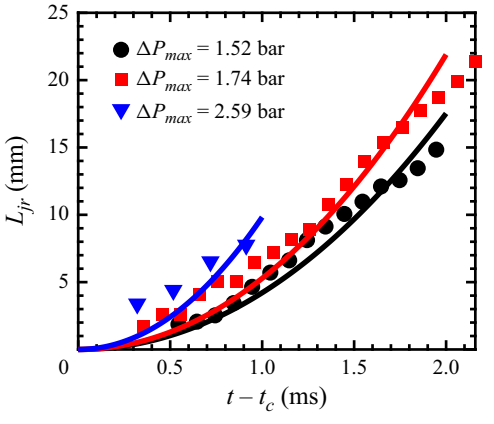



Figure 13. Evolution of the particle jet length from experimental (symbols) and modelling (lines) results.

the growth of $L_{jr}$ in the case with $P_s = 20$ bar and $h = 70$ mm, because the overestimation of $h_c$ in (4.18) results in smaller $a_c$ for this case with a large particle bed thickness.

Figure 12(*b*) demonstrates that the model in (4.21) well captures the growth of $L_{js}$ in the single-mode perturbation cases at various $n$ and $a_{i0}$. Since RMI induces the growth of the particle jet length increment, $L_{js}$ grows faster with larger $n$ and $a_{i0}$ due to a larger pressure perturbation in the RMI.

In the further model assessment, figure 13 shows that the model estimation in (4.20) generally agrees with the experimental results (Xue *et al.* 2018). The parameters used in the comparison between the model estimation in (4.20) and the experimental results are listed in table 2. The critical time $t_c$ is extracted from the experimental data because (4.8) does not hold for the initially loose-packed particle bed ($\Phi_0 = 0.39$) in the experiments. Experimental cases with different pressure histories are fitted with distinct values of $\beta$. Stronger blast waves (larger max overpressure ($\Delta P_{max}$)) compress the particle bed more tightly, resulting in a smaller $h_c$. Thus, a larger $\beta$ is required to correct the overestimated $h_c$ in the model (see Appendix D for details). The fitting parameter $\beta = 1.68$ in the case with $\Delta P_{max} = 1.52$ bar is determined by minimising the mean-squared error



https://doi.org/10.1017/jfm.2025.10807 Published online by Cambridge University Press

| Case | $\Gamma_M$ | $P_s$ (bar) | $t_c$ (ms) | $\beta$ |
|---|---|---|---|---|
| $\Delta P_{max} = 1.52$ bar | 1548 | 2.52 | 3.0 | 1.68 |
| $\Delta P_{max} = 1.74$ bar | 1444 | 3.74 | 3.2 | 1.92 |
| $\Delta P_{max} = 2.59$ bar | 1086 | 3.59 | 3.5 | 2.86 |

Table 2. Summary of the parameters used in our model (4.20) for the experimental cases in Xue *et al.* (2018). Note that $L_{jr}(t_c) = 0$ mm, $R_{I0} = 10$ mm, $h = 20$ mm and $\Phi_0 = 0.39$ are used in modelling all the experimental cases. Since the experiments are in a three-dimensional configuration, the volume fraction of the compacted particle bed is set to $\Phi_{comp} = 0.65$ for modelling all the experimental cases.

between experimental data and model predictions. Subsequent linear fitting yields the relationship $\beta = 1.105\Delta P_{max}/P_0$ , from which the values for cases with $\Delta P_{max} = 1.74$ bar and $\Delta P_{max} = 2.59$ bar are calculated as $\beta = 1.92$ and 2.86, respectively. Moreover, the model slightly overestimates $L_{jr}$ at the late stage. This is because the external surface is penetrated, and then the magnitude of $a_c$ is overestimated in (4.16).

Therefore, the RTI, RMI and large particle inertia lead to the external particle jet formation. The morphological evolution of the dispersed particle bed is dominated by three particle-loosening events: internal particle shedding, external particle jetting and bidirectional particle fingering (Xue *et al.* 2023). For large $P_s$ or small $h$, the internal particle shedding dominates the dispersal process. For large $h$, the bidirectional particle fingering dominates the dispersal process. For small $P_s$, the external particle jet does not occur due to the large particle inertia.

## 5. Conclusions

Through comprehensive analysis of particle dynamics in a radially divergent air-blast-driven dense particle bed, we elucidate the interplay of multiple instability mechanisms governing the evolution of the external particle jet. By examining the cases with random and single-mode perturbations, we reveal that the RTI, RMI and particle inertia collectively drive the particle jet.

The expansion of the particle bed reduces internal gas pressure, subjecting particles near the gas bubble to strong inward coupling forces and variable acceleration motion of RTI. Conversely, particles in the spike region exhibit small gas–particle coupling and collision forces due to their large inertia and low volume fraction, resulting in a near-constant velocity, a distinct departure from the accelerating spikes observed in classical cylindrical RTI.

Further investigation of single-mode perturbations uncovers the role of RMI in the jet length increment. Tracking trough-near particles reveals that perturbation-induced pressure gradients drive their acceleration, enabling them to overtake crest-near particles and induce phase inversion. This process confirms that RMI dominates the growth of the jet length increment. Based on this mechanism, we establish a linear-growth model for the jet length increment, analogous to the planar Richtmyer–Meshkov impulsive model.

By integrating the RMI-based linear-growth model with the baseline RTI-dominated jet dynamics, we propose an external-particle-jet-length model of $L_{js}$ in (4.21), an explicit expression in terms of several parameters. The model parameters consist mainly of two categories: (i) physically derived parameters $V_a$, $t_c$, $h_c$, $k$, $A_m$, $P_0$, $\rho_p$ and $a_{i0}$ obtained from the intrinsic properties of the gas and particle bed; (ii) empirically calibrated parameters $\beta$ and $\Delta U_m$ predetermined through a single case study. This model captures the growth of the external particle jet at moderate initial gas pocket pressures $P_s$ and



https://doi.org/10.1017/jfm.2025.10807 Published online by Cambridge University Press

particle bed thicknesses $h$, and various $n$ and $a_{i0}$, demonstrating good agreements with both numerical simulations and experimental data.

The model sheds light on the control of air-blast induced external particle jets in explosive dispersal granular systems. Increasing the radial velocity $V_a$ accelerates the expansion of the particle ring to promote the jet growth, and preimposed perturbations on the outer interface of the particle bed can further enhance the jet growth. Increasing the thickness $h$ of the particle bed or the particle density $\rho_p$ suppresses the jet growth.

The model of an external particle jet can be further improved in future work. First, under a very strong blast, the particles may break into smaller particles (Frost 2018), making the monodispersed condition invalid. Second, reactive particles such as aluminium powder can be ignited and burn (Posey *et al.* 2021), while only inert particles are considered in the present study. Third, the model is developed based on 2-D cylindrical geometries (three-dimensional (3-D) cylindrical results are shown in Appendix C), so it may need to be adapted for different configurations such as 3-D spherical geometries (Milne *et al.* 2014) in explosive granular dispersal systems. Fourth, the expanding shock distorted by the particle bed generates a velocity perturbation near the gas–particle interface (Huete *et al.* 2021), which should be considered in the future.

**Acknowledgements.** Numerical simulations were carried out on the TH-2A supercomputer in Guangzhou, China.

**Funding.** This work has been supported in part by the National Natural Science Foundation of China (grant nos 12588201, 12432012, 12525201, 12432010 and 12202072) and the Xplore Prize.

**Declaration of interests.** The authors report no conflict of interest.

**Author contributions.** Y.Y., Y.H. and B.T. designed research. Y.H. performed research. All the authors discussed the results and wrote the manuscript. All the authors have given approval for the manuscript.

## Appendix A. Jet formation on a dual-mode interface

To examine mode coupling effects on jet formation, we investigate dual-mode perturbation cases. Based on the random perturbation case with $p = 50$ bar and $h = 50$ mm, the dual-mode case is generated by modifying solely the outer interface of the particle bed as $r = R_{O0} + a_{i0}\sin(n_1\theta) + a_{i0}\sin(n_2\theta + \phi)$, where $n_1$ and $n_2$ denote two circumferential mode numbers, and $\phi$ represents the relative phase between the two modes. Figure 14($a$) depicts the pressure field distribution and calculated particle packet dispersion for the dual-mode case with $n_1 = 9$, $n_2 = 15$ and $\phi = 0$, demonstrating multiple dominant-particle-jet modes protruding from the troughs of the interface.

To investigate the dual-mode perturbation's effects on the growth of the particle jet length, we measure the temporal evolution of jet length increments in the case with $n_1 = 9$, $n_2 = 15$ and $\phi = 0$ and the case with with $n_1 = 9$, $n_2 = 15$ and $\phi = \pi$. In figure 14($b$), $\Delta L_j$ firstly experiences the compression stage because the particles initially near the trough accelerate to move faster than those initially near the crests. After the phase inversion, $\Delta L_j$ in the dual-mode cases also experiences a linear growth. Figure 14($b$) shows that the jet length increment for the two cases with a phase difference of $\pi$ collapses quite well. This suggests a negligible influence of the phases of a dual-mode interface on the growth of jet length increment (Luo *et al.* 2020).

## Appendix B. Linear stability analysis for multiphase RMI

We apply the linear stability analysis for multiphase RMI. We solve the mass and momentum equations of gas and particles in the Euler-Euler form as



https://doi.org/10.1017/jfm.2025.10807 Published online by Cambridge University Press

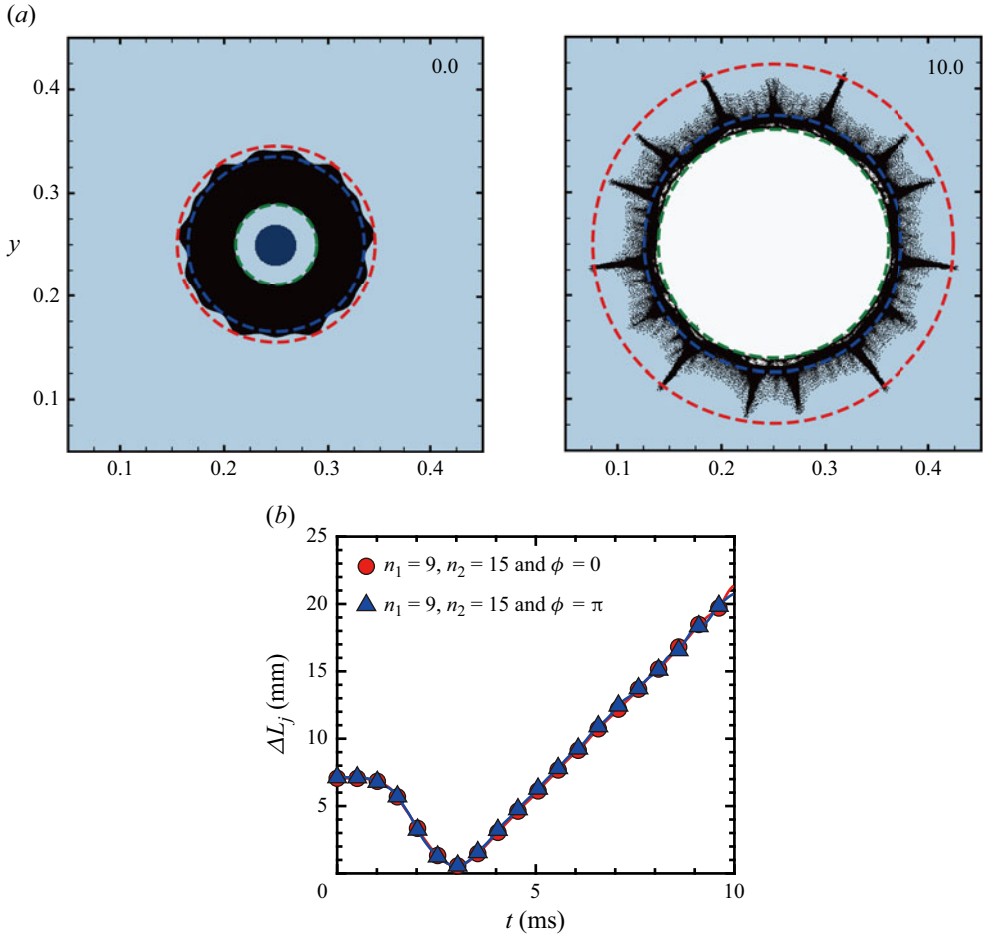



Figure 14. (*a*) Evolution of the particle bed (dots) and the pressure fields (contours) in the dual-mode perturbation case with $n_1 = 9$, $n_2 = 15$ and $\phi = 0$. The colour bar range for the contours corresponds to that of figure 2. The radius of the green, blue and red circles indicate the inner radius $R_I$ of the particle bed, the outer radius $R_C$ of the particle bed and the outer radius $R_O$ of the jet zone, respectively. The numbers in the upper right corner denote the time in ms. The unit of the axes is m. (*b*) Evolution of the particle jet length increment in the dual-mode perturbation cases with various parameters.

$$\frac{\partial \alpha_f \rho_f}{\partial t} + \nabla \cdot \left(\alpha_f \rho_f \boldsymbol{u}_f\right) = 0, \tag{B1}$$

$$\alpha_f \rho_f \left[\frac{\partial \boldsymbol{u}_f}{\partial t} + \left(\boldsymbol{u}_f \cdot \nabla\right) \boldsymbol{u}_f\right] = -\alpha_f \nabla p_f + \alpha_p \rho_p D_p \left(\boldsymbol{v}_p - \boldsymbol{u}_f\right) - \alpha_f \rho_f \boldsymbol{g}_x, \tag{B2}$$

$$\frac{\partial \alpha_p \rho_p}{\partial t} + \nabla \cdot \left(\alpha_p \rho_p \boldsymbol{v}_p\right) = 0, \tag{B3}$$

$$\frac{\partial \boldsymbol{v}_p}{\partial t} + \left(\boldsymbol{v}_p \cdot \nabla\right) \boldsymbol{v}_p = -\frac{1}{\rho_p} \nabla p_f - D_p \left(\boldsymbol{v}_p - \boldsymbol{u}_f\right) - \boldsymbol{g}_x, \tag{B4}$$

where the $x$-direction shock driving acceleration $\boldsymbol{g}_x$ is considered only when the shock passes through the interface. We assume that particles rapidly catch up with the gas,



https://doi.org/10.1017/jfm.2025.10807 Published online by Cambridge University Press

exhibiting minimal overlap and negligible collision forces, justifying the omission of the collision term in (B4). With the same $\rho_p$, the variation of $\alpha_p$ is assumed to be small, and we simplify (B3) into

$$\nabla \cdot \boldsymbol{v}_p = 0. \tag{B5}$$

A physical variable is decomposed into its average and a small perturbation as

$$\left[\boldsymbol{u}_f,\, \boldsymbol{v}_p,\, p_f,\, \alpha_f,\, \alpha_p,\, x\right] = \left[\boldsymbol{U}_0,\, \boldsymbol{U}_0,\, p_{f0},\, \alpha_{f0},\, \alpha_{p0},\, x_0\right] + \left[\boldsymbol{u}'_f,\, \boldsymbol{v}'_p,\, p'_f,\, \alpha',\, -\alpha',\, a_i\right], \tag{B6}$$

where the initial averaged quantities $\boldsymbol{U}_0$, $p_{f0}$, $\alpha_{f0}$ and $\alpha_{p0}$ are $y$-velocity, pressure, volume fraction of the gas phase, and volume fraction of the particle phase, respectively; the superscript $'$ denotes the fluctuation of each variable. Note that due to the incompressibility of particles and the volume conservation, the gas volume fraction varies with $\alpha'$, and the particle volume fraction varies with $-\alpha'$.

Each fluctuation is represented by a 2-D wave:

$$\left[\boldsymbol{u}'_f,\, \boldsymbol{v}'_p,\, p'_f,\, \alpha',\, -\alpha',\, a_i\right] = \left[\hat{\boldsymbol{u}}_f,\, \hat{\boldsymbol{v}}_p,\, \hat{p}_f,\, \hat{\alpha},\, -\hat{\alpha},\, \hat{a}\right] \mathrm{e}^{\mathrm{i}k(y-ct)}, \tag{B7}$$

where the hat denotes the fluctuation amplitude, $k$ the streamwise wavenumber and $c$ the complex phase velocity. Assuming small perturbations and using (B6), (B2) and (B4) can be linearised by

$$\mathrm{i}k\,(U_0 - c)\,\boldsymbol{u}'_f = \left(-\mathrm{i}kp'_f/\rho_f\right) + s\left(\boldsymbol{v}'_p - \boldsymbol{u}'_f\right) - \mathrm{i}kg_x a_i, \tag{B8}$$

$$\mathrm{i}k\,(U_0 - c)\,\boldsymbol{v}'_p = \left(-\mathrm{i}kp'_f/\rho_p\right) + \left(\boldsymbol{u}'_f - \boldsymbol{v}'_p\right)/\tau - \mathrm{i}kg_x a_i, \tag{B9}$$

with $s = D_p\alpha_{p0}\rho_p/(\alpha_{f0}\rho_f)$ and $\tau = 1/D_p$. Combining (B7), (B8) and (B9), we eliminate the particle velocity fluctuation $\boldsymbol{v}'_p$ and obtain the pressure perturbation amplitude

$$\hat{p}_f = \left[ik\left(\frac{Q_b}{\rho_f} + \frac{s}{\rho_p}\right)\right]^{-1}\left\{\left(\frac{s}{\tau} - Q_a Q_b\right)\hat{\boldsymbol{u}}_f - \mathrm{i}kg_x\,(Q_b + s)\,\hat{a}\right\}, \tag{B10}$$

with $Q_a = \mathrm{i}k(U_0 - c) + s$ and $Q_b = \mathrm{i}k(U_0 - c) + 1/\tau$.

With a similar derivation in Meng *et al.* (2019), we obtain the general expression of the RTI and RMI by applying the pressure equilibrium condition to (B10) on the perturbed interface:

$$\begin{aligned}
&\left[i\frac{k(U_0 - c)}{\rho_{f2}} + \frac{1}{\tau_2\rho_{f2}} + \frac{s_2}{\rho_{p2}}\right]\left\{i\left[k^2(U_0 - c)^3 - g_x k(U_0 - c)\right]\right.\\
&\left.+\left(s_1 + \frac{1}{\tau_1}\right)\left[-g_x + k(U_0 - c)^2\right]\right\}\\
&=\left[i\frac{k(U_0 - c)}{\rho_{f1}} + \frac{1}{\tau_1\rho_{f1}} + \frac{s_1}{\rho_{p1}}\right]\left\{i\left[-k^2(U_0 - c)^3 - g_x k(U_0 - c)\right]\right.\\
&\left.+\left(s_2 + \frac{1}{\tau_2}\right)\left[-g_x - k(U_0 - c)^2\right]\right\},
\end{aligned} \tag{B11}$$

where subscripts 1 and 2 correspond to physical quantities in the upstream and downstream, respectively. Since the base flow in RTI and RMI is initially at rest (Ukai *et al.* 2010), $U_0 = 0$ is applied in (B11). The assumption of excellent particle-tracking capability implies sufficiently large values of $s$ and $\tau^{-1}$, thereby justifying retaining only



https://doi.org/10.1017/jfm.2025.10807 Published online by Cambridge University Press

the terms involving $s$ and $\tau^{-1}$ in (B11). Therefore, (B11) is simplified as

$$\left(\frac{1}{\tau_2\rho_{f2}}+\frac{s_2}{\rho_{p2}}\right)\left(s_1+\frac{1}{\tau_1}\right)\left(g_x-kc^2\right)=\left(\frac{1}{\tau_1\rho_{f1}}+\frac{s_1}{\rho_{p1}}\right)\left(s_2+\frac{1}{\tau_2}\right)\left(g_x+kc^2\right), \tag{B12}$$

and arrives at

$$c^2=-\frac{g_x}{k}A_m,\quad A_m=\frac{\bar{\rho}_2-\bar{\rho}_1}{\bar{\rho}_2+\bar{\rho}_1},\quad \frac{1}{\bar{\rho}_j}=\frac{1}{s_j+\frac{1}{\tau_j}}\left(\frac{1/\tau_j}{\rho_{fj}}+\frac{s_j}{\rho_{pj}}\right),\quad j=1,2. \tag{B13}$$

Substituting the definitions of $s$ and $\tau$ in (B8) and (B9) into (B13), we obtain

$$A_m=\frac{\left(\rho_{f2}\alpha_{f2}+\rho_{p2}\alpha_{p2}\right)-\left(\rho_{f1}\alpha_{f1}+\rho_{p1}\alpha_{p1}\right)}{\left(\rho_{f2}\alpha_{f2}+\rho_{p2}\alpha_{p2}\right)+\left(\rho_{f1}\alpha_{f1}+\rho_{p1}\alpha_{p1}\right)}. \tag{B14}$$

The growth rate of the perturbed interface is given by (B7):

$$\frac{\mathrm{d}^2a_i}{\mathrm{d}t^2}=-k^2c^2a_i(t). \tag{B15}$$

Combining with (B16) yields

$$\frac{\mathrm{d}^2a_i}{\mathrm{d}t^2}=ka_i(t)A_mg_x, \tag{B16}$$

which is the linear growth rate for the RTI. Integrating (B16) with respect to time, we obtain the linear-growth model for multiphase RMI:

$$\dot{a}_i=ka_{i0}A_m\Delta U_m. \tag{B17}$$

## Appendix C. Simulation results for the 3-D cylindrical cases

We consider a 3-D cylindrical configuration that maintains geometric similarity to the experimental arrangement of a Hele-Shaw cell (Xue *et al.* 2018). This configuration is simulated in the 3-D domain $\mathcal{D}=[0,\,W_x]\times[0,\,W_y]\times[0,\,W_z]$, with domain sizes $W_x$, $W_y$ and $W_z$ in the $x$-, $y$- and $z$-directions. The 3-D computational domain is discretised on $512\times512\times4$ uniform grid points with mesh spacing $\Delta x=1.00$ mm. Outflow boundary conditions are applied in the $x$- and $y$-directions, while a wall boundary condition is applied in the $z$-direction. Both the gas pocket and the particle bed are set at the domain centre $(x_c,\,y_c,\,z_c)=(W_x/2,\,W_y/2,\,W_z/2)$. The annular particle bed with initial volume fraction $\Phi_0=0.52$ is filled by random distributed computational parcels (Lozano *et al.* 2016). Approximately 700 000 parcels are utilised in the simulation. The particles possess physical properties identical to those in the 2-D simulation case. Particle–wall collisions are modelled using the soft-sphere model in (2.3), with the wall stiffness coefficient assumed identical to that of the particles.

Two cases are simulated in 3-D cylindrical configuration: the single-mode perturbation case with $n=12$ and $a_{i0}=2.4$ mm and the random perturbation case with $P_s=20$ bar and $h=50$ mm. The contour plot of gas pressure and position of the computational parcels are shown in figure 15. The 3-D computational results exhibit features comparable to 2-D simulations, including central pressure reduction below ambient pressure and a dominant mode observed in the single-mode case. Consequently, the conclusions drawn in the present study can be generalised to scenarios involving 3-D cylindrical geometries.

We quantify the external particle jet length by measuring characteristic radii with circumferentially averaged particle volume fractions. The circles in figures 15(*a*) and 15(*b*)



https://doi.org/10.1017/jfm.2025.10807 Published online by Cambridge University Press

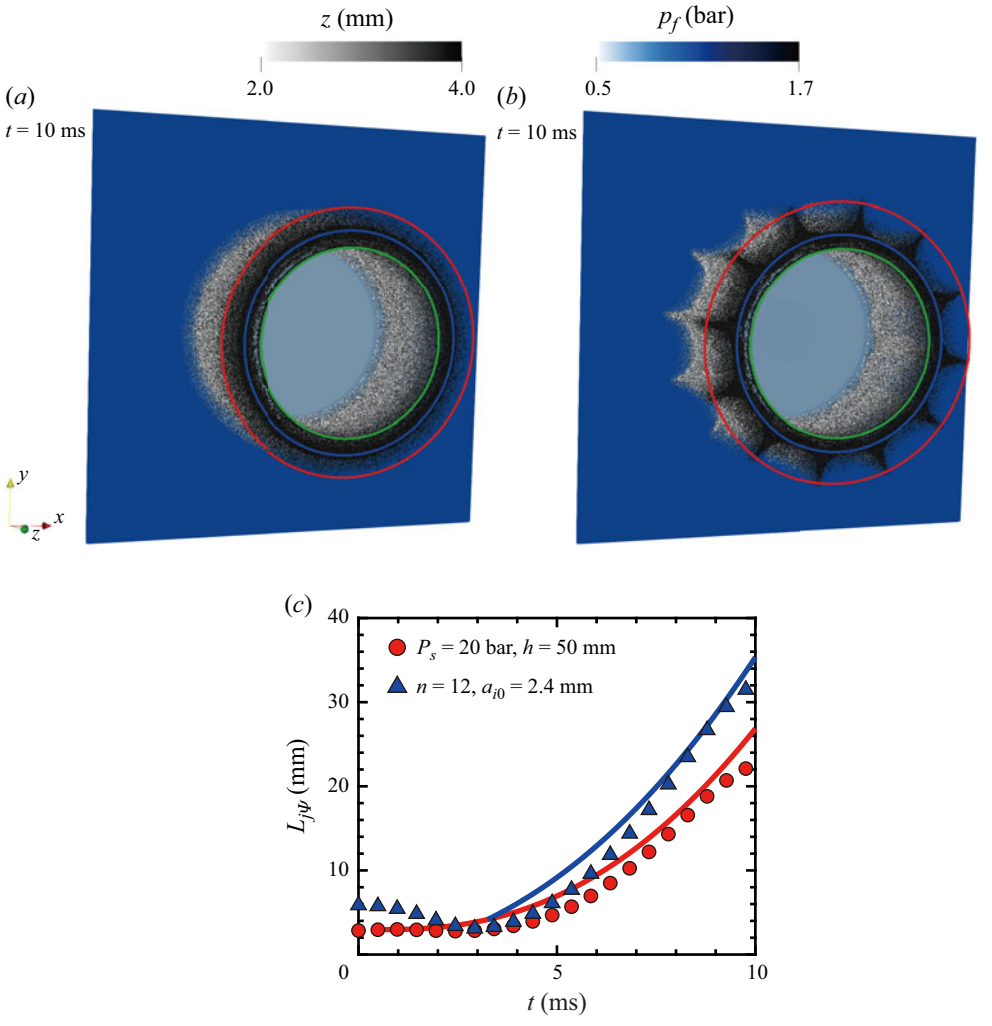



Figure 15. Evolution of the particle bed (dots) and the pressure fields (contours) in (*a*) the single-mode perturbation case with $n = 12$ and $a_{i0} = 2.4$ mm and (*b*) the random perturbation case with $P_s = 20$ bar and $h = 50$ mm. The green, blue and red circles indicate the inner radius $R_I$ of the particle bed, the outer radius $R_C$ of the particle bed and the outer radius $R_O$ of the jet zone, respectively. Note that the configuration has been stretched by a factor of 50 along the $z$-axis to enhance visibility of the 3-D structure. (*c*) Evolution of the particle jet length from numerical simulation (symbols) and modelling (lines) results.

demonstrate that the characteristic radii capture the structures of the particle bed and the external particle jet well. Figure 15(*c*) demonstrates that the evolution of external particle jets in the 3-D geometry is similar to that observed in 2-D, where the single-mode perturbation triggers RMI, inducing $\Delta L_j$. Furthermore, the model results in (4.20) and (4.21) with $\Phi_{comp} = 0.55$, and the fitting parameters $\beta = 1.0$ and $\Delta U_m = 4.0\ \mathrm{m\ s^{-1}}$ generally agree with the simulation results of the 3-D cylindrical configurations. In the 3-D case, $\Phi_{comp}$ is lower than in 2-D (Zhang, Damjanac & Huang 2013), resulting in a larger $h_c$ and a smaller $a_c$. Consequently, the growth rate of particle jet length in 3-D is slower compared with that in 2-D.



https://doi.org/10.1017/jfm.2025.10807 Published online by Cambridge University Press

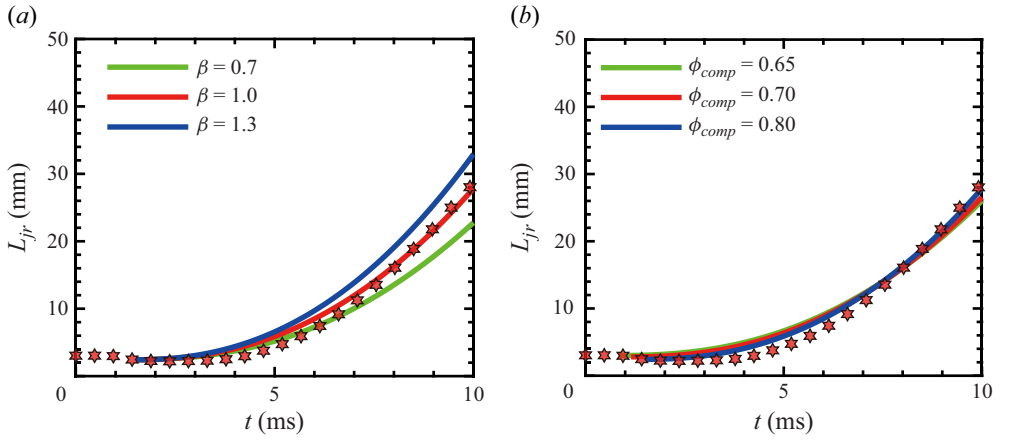



Figure 16. Evolution of the particle jet length from numerical simulation (symbols) and modelling (lines) results with different (*a*) $\beta$ and (*b*) $\phi_{comp}$ in the random perturbation case with $P_s = 20$ bar and $h = 50$ mm.

## Appendix D. Sensitive analysis of the external-particle-jet-length model

We conducted sensitive analysis for the empirical parameters in the external-particle-jet-length model in (4.20), using the random perturbation case with $P_s = 20$ bar and $h = 50$ mm. Figure 16(*a*) demonstrates that a larger $\beta$ leads to a greater predicted $L_{jr}$ by the model. This indicates that overestimation or underestimation of $h_c$ in (4.16) can be corrected by increasing or decreasing $\beta$, respectively. Figure 16(*b*) shows that different values of $\Phi_{comp}$ primarily affect $t_c$, but have minimal effects on predicting the growth of $L_{jr}$.

## References


Annamalai, S., Rollin, B., Ouellet, F., Neal, C., Jackson, T.L. & Balachandar, S. 2016 Effects of initial perturbations in the early moments of an explosive dispersal of particles. *J. Fluids Engng.* **138**, 070903.

Baer, M.R. & Nunziato, J.W. 1986 A two–phase mixture theory for the deflagration–to–detonation transition (ddt) in reactive granular materials. *Int. J. Multiph. Flow* **12**, 861–889.

Balakrishnan, K. & Menon, S. 2010 On turbulent chemical explosions into dilute aluminum particle clouds. *Combust. Theory Model.* **14**, 583–617.

Barba, F.D. & Picano, F. 2018 Clustering and entrainment effects on the evaporation of dilute droplets in a turbulent jet. *Phys. Rev. Fluids* **3** (3), 034304.

Bell, G.I. 1951 *Taylor instability on cylinders and spheres in the small amplitude approximation*. Report No. LA-1321, LANL. vol. **1321**, pp. 91873–91879,

Bender, J.D. *et al.* 2021 Simulation and flow physics of a shocked and reshocked high–energy–density mixing layer. *J. Fluids Mech.* **915**, A84.

Berk, T. & Coletti, F. 2021 Dynamics of small heavy particles in homogeneous turbulence: a Lagrangian experimental study. *J. Fluids Mech.* **917**, A47.

Britan, A. & Ben-Dor, G. 2006 Shock tube study of the dynamical behavior of granular materials. *Int. J. Multiph. Flow* **32**, 623–642.

Calvo-Rivera, A., Huete, C. & Velikovich, A.L. 2022 The stability of expanding reactive shocks in a van der Waals fluid. *Phys. Fluids* **34** (4), 046106.

Calvo-Rivera, A., Velikovich, A.L. & Huete, C. 2023 On the stability of piston-driven planar shocks. *J. Fluids Mech.* **964**, A33.

Capecelatro, J. 2022 Modeling high–speed gas–particle flows relevant to spacecraft landings. *Int. J. Multiph. Flow* **150**, 104008.

Capecelatro, J. & Desjardins, O. 2013 Eulerian–Lagrangian modeling of turbulent liquid–solid slurries in horizontal pipes. *J. Comput. Phys.* **55**, 64–79.




https://doi.org/10.1017/jfm.2025.10807 Published online by Cambridge University Press

CAPECELATRO, J. & WAGNER, J.L. 2024 Gas–particle dynamics in high–speed flows. *Annu. Rev. Fluid Mech.* **56**, 379–403.
CHIAPOLINO, A. & SAUREL, R. 2020 Numerical investigations of two–phase finger–like instabilities. *Comput. Fluids* **206**, 104585.
CROWE, C., SOMMERFIELD, M. & TSUJI, Y. 1998 *Multiphase Flows with Droplets and Particles*. CRC Press.
CROWL, D.A. 2003 *Understanding Explosions*. Wiley.
DING, J., FAN, C., ZHOU, Z. & LUO, X. 2025 Instability at imploding gas layer impacted by convergent shock. *J. Fluids Mech.* **1008**, A9.
DING, J., SI, T., YANG, J., LU, X., ZHAI, Z. & LUO, X. 2017 Measurement of a Richtmyer–Meshkov instability at an air-SF 6 interface in a semiannular shock tube. *Phys. Rev. Lett.* **119**, 014501.
FERNÁNDEZ-GODINO, M.G., OUELLET, F., HAFTKA, R.T. & BALACHANDAR, S. 2019 Early time evolution of circumferential perturbation of initial particle volume fraction in explosive cylindrical multiphase dispersion. *J. Fluids Engng.* **141**, 091302.
FROST, D.L. 2018 Heterogeneous/particle–laden blast waves. *Shock Waves* **28**, 439–449.
FROST, D.L., GRÉGOIRE, Y., PETEL, O., GOROSHIN, S. & ZHANG, F. 2012 Particle jet formation during explosive dispersal of solid particles. *Phys. Fluids* **24**, 091109.
HE, Y., MENG, B., TIAN, B. & YANG, Y. 2024 Shock–induced instability of dual–layer dilute gas–particle mixture. *Phys. Rev. Fluids* **9**, 124301.
HE, Y., PENG, N., LI, H., TIAN, B. & YANG, Y. 2023 Formation of the cavity on a planar interface subjected to a perturbed shock wave. *Phys. Rev. Fluids* **8** (6), 063402.
HUETE, C., VELIKOVICH, A.L., MARTINEZ-RUIZ, D. & CALVO-RIVERA, A. 2021 Stability of expanding accretion shocks for an arbitrary equation of state. *J. Fluids Mech.* **927**, A34.
HUGHES, K.T., BALACHANDAR, S., DIGGS, A., HAFTKA, R., KIM, N.H. & LITTRELL, D. 2020 Simulation–driven design of experiments examining the large–scale, explosive dispersal of particles. *Shock Waves* **30**, 325–347.
HUGHES, K.T., CHARONKO, J.J., PRESTRIDGE, K.P., KIM, N.H., HAFTKA, R.T. & BALACHANDAR, S. 2021 Proton radiography of explosively dispersed metal particles with varying volume fraction and varying carrier phase. *Shock Waves* **31**, 75–88.
KONERU, R.B., ROLLIN, B., DURANT, B., OUELLET, F. & BALACHANDAR, S. 2020 A numerical study of particle jetting in a dense particle bed driven by an air–blast. *Phys. Fluids* **32**, 093301.
LAI, S., HOUIM, R.W. & ORAN, E.S. 2018 Effects of particle size and density on dust dispersion behind a moving shock. *Phys. Rev. Fluids* **3**, 064306.
LI, J., DING, J., SI, T. & LUO, X. 2020 Convergent Richtmyer–Meshkov instability of light gas layer with perturbed outer surface. *J. Fluids Mech.* **884**, R2.
LI, J., XUE, K., ZENG, J., TIAN, B. & GUO, X. 2022 Shock–induced interfacial instabilities of granular media. *J. Fluid Mech.* **930**, A22.
LI, J., WANG, H., ZHAI, Z. & LUO, X. 2023*a* Richtmyer–Meshkov instability of a single–mode heavy–light interface in cylindrical geometry. *Phys. Fluids* **35**, 106112.
LI, J., ZENG, J. & XUE, K. 2023*b* Pressure evolution in shock–compacted granular media. *Pet. Sci.* **20** (6), 3736–3751.
LIU, H., TAFTI, D.K. & LI, T. 2014 Hybrid parallelism in MFIX CFD–DEM using OpenMP. *Powder Technol.* **259**, 22–29.
LOTH, E. 2008 Compressibility and rarefaction effects on drag of a spherical particle. *AIAA J.* **46**, 2219–2228.
LOZANO, E., ROEHL, D., CELES, W. & GATTASS, M. 2016 An efficient algorithm to generate random sphere packs in arbitrary domains. *Comput. Math. Appl.* **71**, 1586–1601.
LUBE, G., BREARD, E.C.P., ESPOSTI-ONGARO, T., DUFEK, J. & BRAND, B. 2020 Multiphase flow behaviour and hazard prediction of pyroclastic density currents. *Nat. Rev. Earth Environ.* **1** (7), 348–365.
LUO, X., LIU, L., LIANG, Y., DING, J. & WEN, C. 2020 Richtmyer–Meshkov instability on a dual–mode interface. *J. Fluids Mech.* **905**, A5.
MCFARLAND, J.A., BLACK, W.J., DAHAL, J. & MORGAN, B.E. 2016 Computational study of the shock driven instability of a multiphase particle–gas system. *Phys. Fluids* **28**, 024105.
MCGRATH, T.P., CLAIR, J.G.S. & BALACHANDAR, S. 2016 A compressible two–phase model for dispersed particle flows with application from dense to dilute regimes. *J. Appl. Phys.* **119**, 174903.
MENG, B., ZENG, J., TIAN, B., LI, L., HE, Z. & GUO, X. 2019 Modeling and verification of the Richtmyer–Meshkov instability linear growth rate of the dense gas-particle flow. *Phys. Fluids* **31** (7), 074102.
MESHKOV, E.E. 1969 Instability of the interface of two gases accelerated by a shock wave. *Fluid Dyn.* **4**, 101–104.
MICHAEL, D.H. 1965 Kelvin–Helmholtz instability of a dusty gas. *Math. Proc. Camb. Philos. Soc.* **61**, 569–571.

https://doi.org/10.1017/jfm.2025.10807 Published online by Cambridge University Press

MIDDLEBROOKS, J.B., AVGOUSTOPOULOS, C.G., BLACK, W.J., ALLEN, R.C. & MCFARLAND, J.A. 2018 Droplet and multiphase effects in a shock-driven hydrodynamic instability with reshock. *Exp. Fluids* **59** (98), 1–16.

MIKAELIAN, K.O. 2005 Rayleigh–Taylor and Richtmyer–Meshkov instabilities and mixing in stratified cylindrical shells. *Phys. Fluids* **17**, 094105.

MILNE, A.M. 2016 Gurney analysis of porous shells. *Propellants Explos. Pyrotech.* **41**, 665–671.

MILNE, A., PARRISH, C. & WORLAND, I. 2010 Dynamic fragmentation of blast mitigants. *Shock Waves* **20**, 41–51.

MILNE, A.M., FLOYD, E., LONGBOTTOM, A.W. & TAYLOR, P. 2014 Dynamic fragmentation of powders in spherical geometry. *Shock Waves* **24**, 501–513.

OSNES, A.N., VARTDAL, M., KHALLOUFI, M., CAPECELATRO, J. & BALACHANDAR, S. 2023 Comprehensive quasi-steady force correlations for compressible flow through random particle suspensions. *Int. J. Multiph. Flow* **165**, 104485.

OSNES, A.N., VARTDAL, M. & REIF, B.A.P. 2018 Numerical simulation of particle jet formation induced by shock wave acceleration in a Hele-Shaw cell. *Shock Waves* **28**, 451–461.

PAPALEXANDRIS, M.V. 2004 Numerical simulation of detonations in mixtures of gases and solid particles. *J. Fluids Mech.* **507**, 95–142.

PENG, N., YANG, Y., WU, J. & XIAO, Z. 2021*a* Mechanism and modelling of the secondary baroclinic vorticity in the Richtmyer–Meshkov instability. *J. Fluids Mech.* **911**, A56.

PENG, N., YANG, Y. & XIAO, Z. 2021*b* Effects of the secondary baroclinic vorticity on the energy cascade in the Richtmyer–Meshkov instability. *J. Fluids Mech.* **925**, A39.

PONTALIER, Q., LOISEAU, J., GOROSHIN, S. & FROST, D.L. 2018 Experimental investigation of blast mitigation and particle–blast interaction during the explosive dispersal of particles and liquids. *Shock Waves* **28**, 489–511.

POSEY, J.W., ROQUE, B., GUHATHAKURTA, S. & HOUIM, R.W. 2021 Mechanisms of prompt and delayed ignition and combustion of explosively dispersed aluminum powder. *Phys. Fluids* **33**, 113308.

RANA, U., ABADIE, T., CHAPMAN, D., JOINER, N. & MATAR, O.K. 2024 Richtmyer–Meshkov instability at high Mach number: non–Newtonian effects. *Phys. Fluids* **36**, 066104.

RENZO, A.D., NAPOLITANO, E.S. & MAIO, F.P.D. 2021 Coarse–grain dem modelling in fluidized bed simulation: a review. *Processes* **9** (2), 279.

RICHTMYER, R.D. 1960 Taylor instability in shock acceleration of compressible fluids. *Commun. Pure Appl. Maths* **13**, 297–319.

RODRIGUEZ, V., SAUREL, R., JOURDAN, G. & HOUAS, L. 2013 Solid–particle jet formation under shock-wave acceleration. *Phys. Rev. E* **88**, 063011.

RODRIGUEZ, V., SAUREL, R., JOURDAN, G. & HOUAS, L. 2014 External front instabilities induced by a shocked particle ring. *Phys. Rev. E* **90**, 043013.

RODRIGUEZ, V., SAUREL, R., JOURDAN, G. & HOUAS, L. 2017 Impulsive dispersion of a granular layer by a weak blast wave. *Shock Waves* **27**, 187–198.

ROGUE, X., RODRIGUEZ, G., HAAS, J.F. & SAUREL, R. 1998 Experimental and numerical investigation of the shock–induced fluidization of a particles bed. *Shock Waves* **8**, 29–45.

SHALLCROSS, G.S., FOX, R.O. & CAPECELATRO, J. 2020 A volume–filtered description of compressible particle–laden flows. *Int. J. Multiph. Flow* **122**, 103138.

SI, T., JIANG, S., CAI, W., WANG, H. & LUO, X. 2025 Shock–tube experiments on strong–shock–driven single–mode Richtmyer–Meshkov instability. *J. Fluids Mech.* **1006**, R1.

TIAN, B., ZENG, J., MENG, B., CHEN, Q., GUO, X. & XUE, K. 2020 Compressible multiphase particle–in–cell method (CMP-PIC) for full pattern flows of gas-particle system. *J. Comput. Phys.* **418**, 109602.

UKAI, S., BALAKRISHNAN, K. & MENON, S. 2010 On Richtmyer–Meshkov instability in dilute gas–particle mixtures. *Phys. Fluids* **22**, 104103.

VOROBIEFF, P., ANDERSON, M., CONROY, J., WHITE, R., TRUMAN, C.R. & KUMAR, S. 2011 Vortex formation in a shock–accelerated gas induced by particle seeding. *Phys. Rev. Lett.* **106** (18), 184503.

WANG, Z., LIU, M. & YANG, X. 2020 A four-way coupled CFD-DEM modeling framework for charged particles under electrical field with applications to gas insulated switchgears. *Powder Technol.* **373**, 433–445.

XUE, K., DU, K., SHI, X., GAN, Y. & BAI, C. 2018 Dual hierarchical particle jetting of a particle ring undergoing radial explosion. *Soft Matter* **14**, 4422–4431.

XUE, K., MIU, L., LI, J., BAI, C. & TIAN, B. 2023 Explosive dispersal of granular media. *J. Fluid Mech.* **959**, A17.

XUE, K., SUN, L. & BAI, C. 2016 Formation mechanism of shock–induced particle jetting. *Phys. Rev. E.* **94** (2), 022903.



https://doi.org/10.1017/jfm.2025.10807 Published online by Cambridge University Press

ZENG, J., MENG, B., YE, X. & TIAN, B. 2024 Closed equation model for cavity evolution in granular media. *J. Fluids Mech.* **996**, A15.

ZHANG, F., DAMJANAC, B. & HUANG, H. 2013 Coupled discrete element modeling of fluid injection into dense granular media. *J. Geophys. Res.-Solid Earth* **118**, 2703–2722.

ZHANG, F., FROST, D.L., THIBAULT, P.A. & MURRAY, S.B. 2001 Explosive dispersal of solid particles. *Shock Waves* **10** (6), 431–443.

ZHANG, F., RIPLEY, R.C., YOSHINAKA, A., FINDLAY, C.R., ANDERSON, J. & ROSEN, B.V. 2015 Large–scale spray detonation and related particle jetting instability phenomenon. *Shock Waves* **25**, 239–254.

ZHOU, Y. 2017*a* Rayleigh–Taylor and Richtmyer–Meshkov instability induced flow, turbulence, and mixing. I. *Phys. Rep.* **720–722**, 1–136.

ZHOU, Y. 2017*b* Rayleigh–Taylor and Richtmyer–Meshkov instability induced flow, turbulence, and mixing. II. *Phys. Rep.* **723–725**, 1–160.

ZHOU, Y. *et al.* 2021 Rayleigh–Taylor and Richtmyer–Meshkov instabilities: a journey through scales. *Physica D* **423**, 132838.

ZOU, L., LIU, J., LIAO, S., ZHENG, X., ZHAI, Z. & LUO, X. 2017 Richtmyer–Meshkov instability of a flat interface subjected to a rippled shock wave. *Phys. Rev. E* **95**, 013107.

https://doi.org/10.1017/jfm.2025.10807 Published online by Cambridge University Press